Erasmus Mundus
JMD on
Nuclear Physics

Laser Spectroscopy of Neutron Deficit Pd

Saikumar Chinthakayala

UNICAEN

GANIL
spiral2
laboratoire commun CEA/DSM   CNRS/IN2P3

Supervisor: Dr. Lucia Caceres

Master Thesis Report
Erasmus Mundus Joint Master Degree
in Nuclear Physics

Dr. Lucia Caceres

Contents

List of Figures

List of Tables

1 | Introduction

Atomic nucleus is a complex many body system composed of protons and neutrons. Studying the nature of interaction between nucleons is primordial for the understanding of nuclear force. Laser spectroscopy is one of the widely utilized techniques for nuclear structure studies. It involves investigating atomic transitions which occur on the order of a few electron volts. Along the isotopic chain of a given nucleus, the atomic energy levels are slightly perturbed due to the interactions between the atomic nucleus and the electrons. As this method is capable of detecting changes in these transitions at the parts-per-million (ppm) level, it becomes a highly sensitive tool for probing the atomic levels and thus nuclear properties. Measurement of isotope shifts and atomic hyperfine structure allows model independent determination of magnetic dipole moment, spectroscopic electric quadrupole moment, the relative change in mean squared charge radius and the nuclear spin. These properties will be defined in the sections that follow.

The determination of nuclear properties in the region around ^{100}Sn is not only an interesting but a challenging task in the field of laser spectroscopy. ^{100}Sn is a doubly magic and self-conjugate nucleus with equal numbers of protons and neutrons (N = Z = 50). This makes it a valuable benchmark for testing state-of-the-art nuclear models and understanding the nuclear many-body problem [14]. Additionally, studying the nuclei in this region is challenging because isotopes are extremely short-lived. However, thanks to advancements in radioactive ion production and precision techniques, it has become possible to overcome these challenges and study these nuclei in detail. [10, 15, 16]

The local evolution of nuclear properties around N=Z line provides a better insight into nucleon-nucleon interaction. When neutrons and protons occupy identical orbitals, they show strong nucleon correlations. This is expected to manifest in various nuclear properties like mass, excitation energies, shape, size etc. Since these nuclei are also close to the proton drip line, the coupling to continuum states effects the nuclear structure. [17]. Moreover, shell closure effects can be studied crossing the N = 50 magic number.

Figure 1.1 shows the changes in nuclear charge radii when crossing the N = 50 magic number. A sudden change in the smooth trend reflects the nuclear structure/shell effects on the charge radius. Particularly in the case of Ag, the discontinuity could not be reproduced by existing nuclear models. The question that follows is then how pronounced the shift in nuclear charge radii is when reducing Z. Focusing on Pd, the most neutron deficit isotope explored till now contains 52 neutrons [2]. To reach the lighter Pd isotopes two different but complementary laser spectroscopy techniques are foreseen.

The first method is an efficient in-source resonant ionization spectroscopy in a hot-cavity catcher coupled to collinear laser spectroscopy set-up with MR-ToF MS (Multiple Reflection Time of Flight Mass Spectrometer) as a precise ion detector at IGISOL facility, Jyvaskyla. Using a similar technique, promising results have been achieved in the optical measurements of neutron deficit ^{96}Ag isotope with on-resonance signal rates as low as 0.005 ions per second [4]. Figure 1.2 shows that the same technique can be used to study nuclei till ^{93}Pd.

The second method is to use in-gas laser spectroscopy combined with MR-ToF mass spectrometer at the upcoming S3-LEB facility at GANIL [12] which should offer a better resolution than the aforementioned technique. According to the predicted yields, the beams will have sufficient counting rates to study the Pd isotopes of interest. In this report, the preparatory studies to perform the above mentioned experiments are reported.

In chapter 1, a compact introduction is presented, covering various nuclear properties such as the relative mean square charge radius, magnetic dipole moment, and electric quadrupole moment. Additionally, the chapter explores atomic theory, isotope shift, and hyperfine spectra. It ends with a section on development of hyperfine spectra simulator.

Analysis of existing fluorescence data of few Pd isotopes is presented in chapter 2. Development of new efficient resonant ionisation scheme for Pd involves designing, alignment and tuning of laser cavities. Concise laser theory, types of lasers, frequency selection optical elements and laser alignment of a broadband cavity at GISELE laboratory is presented in chapter 3. The final chapter presents the development and testing of a GUI based software for PILGRIM MR-ToF MS for online data acquisition.
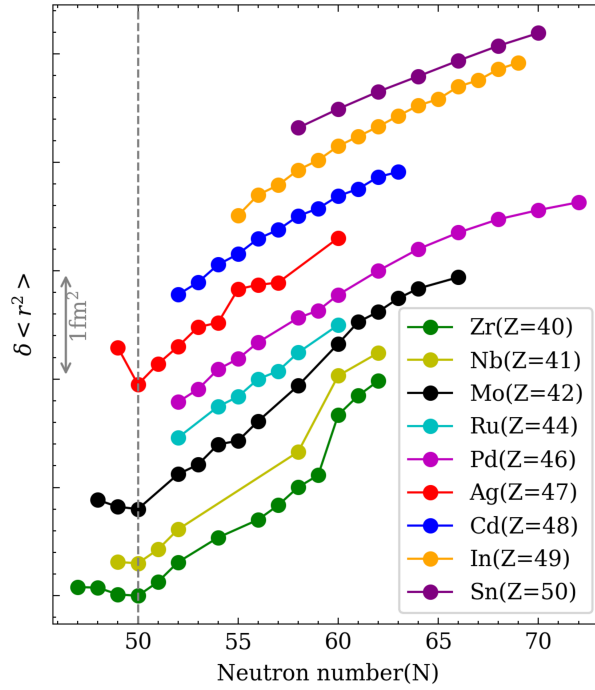
Figure 1.1: Overview of changes in root mean square charge radii as a function of neutron number (N) in the region of Mo to Sn region [1,2,3]. Data of each element is arbitrarily offset for a better clarity
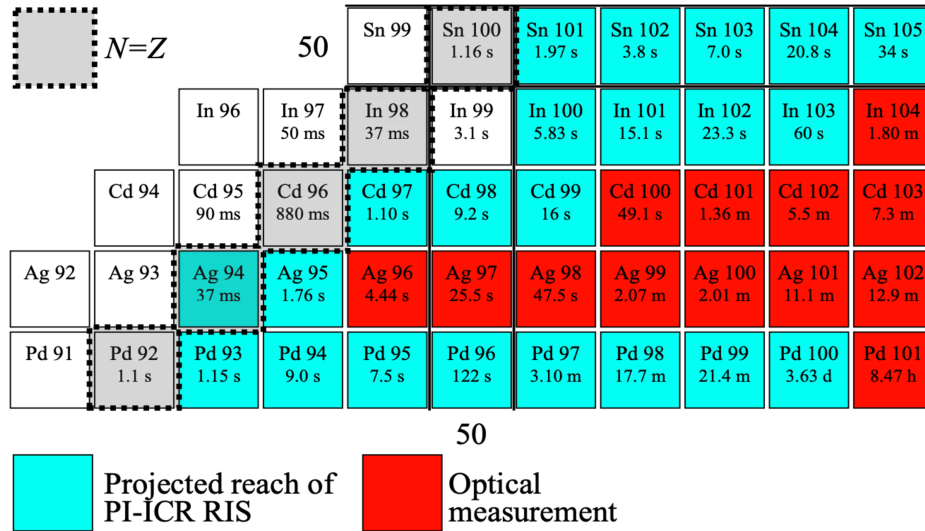

Figure 1.2: Various nuclei that can be studied using PI-ICR -assisted RIS technique [4]

1.1 Atomic Theory and Nuclear Properties

Bohr's theory was one of the first models to explain the atomic spectra using quantization of angular momentum. Quantum mechanics was further used to solve hydrogen atom problem.

Time dependent Schrodinger's equation is given as:

$$\hat{H}\psi(r_1, r_2; t) = i\hbar \frac{\partial \psi(r_1, r_2; t)}{\partial t} \tag{1.1}$$

$$\left[-\frac{\hbar^2}{2m_1}\nabla_1^2 - \frac{\hbar^2}{2m_1}\nabla_1^2 + V(\overrightarrow{r}_1, \overrightarrow{r}_2; t)\right]\psi(r_1, r_2; t) = i\hbar \frac{\partial \psi(r_1, r_2; t)}{\partial t} \tag{1.2}$$

where r_1 and r_2 denote the positions of proton and electron in a hydrogen atom with respect to origin. Co-ordinate transformation to the centre of mass system modifies the equation as,

$$-\frac{\hbar^2}{2M}\nabla_R^2 \chi(\overrightarrow{R}) = E_R \chi(\overrightarrow{R}) \tag{1.3}$$

$$\left[-\frac{\hbar^2}{2\mu}\nabla_r^2 + V(\overrightarrow{r})\right]\phi(\overrightarrow{r}) = E_r \phi(\overrightarrow{r}) \tag{1.4}$$

where $\overrightarrow{r}$ denotes relative distance between electron and proton and $\overrightarrow{R}$ denotes the distance of centre of mass from the origin.

Assuming a central potential, $V = V(\overrightarrow{r})$ allows separating the wave function into radial and angular part. Upon solving, spherical harmonic solutions are obtained for angular part and Laguerre polynomial solutions for the radial parts of the wave function. From the radial solution, the Eigen energies for hydrogen-like atoms are obtained as

$$E_n = \frac{-Z^2}{n^2} \times 13.6 eV \tag{1.5}$$

where n is principal quantum number (n = 1,2,3,..) and Z is the atomic number.

Observations of fine structure in atomic hydrogen spectra using high resolution spectrometers led to corrections in original Hamiltonian to match the experimental data.

$$\hat{H}_{fs} = \underbrace{\frac{\hat{p}^2}{2\mu} - \frac{1}{4\pi\epsilon_0}\frac{Ze^2}{r}}_{H_O} - \underbrace{\frac{p^4}{8\mu^3 c^2}}_{Rel.Cor} + \underbrace{\frac{\pi\hbar^2}{2\mu^2 c^2}\frac{Ze^2}{4\pi\epsilon_0}\delta^3(\overrightarrow{r})}_{Darwin} + \underbrace{\frac{1}{2\mu^2 c^2 r}\frac{dV}{dr}\overrightarrow{l}.\overrightarrow{s}}_{SO-Coupling} \tag{1.6}$$

where two terms in the beginning of the Equation 1.6 are from original Hamiltonian and the relativistic correction is represented in third term, finite size of electron is also included as Darwin term. The final term is from spin orbit coupling orbital angular momentum ($\overrightarrow{l}$) and its intrinsic spin ($\overrightarrow{s}$) of the electron which lifts the degeneracy of atomic levels. The above Hamiltonian cannot be solved analytically, therefore time independent perturbation theory is used to obtain approximate solutions. The eigen energies are then expressed as:

$$E_{fs} = 13.6 \times Z^4 \times \frac{1}{137^2 \times n^3}\left[\frac{1}{j+1/2} - \frac{3}{4n}\right] \tag{1.7}$$

where j is the total angular momentum of the electron. For multi electronic systems the formalism involves mean field approximations [18].

The basic properties of nucleus further perturb the atomic energy levels causing noticeable shifts or splittings in the fine atomic spectra. These shifts or splittings typically occur at the scale of 10^{-3}eV to 10^{-7}eV (100 GHz - 10 MHz). As advancements in experimental techniques have continuously enhanced the precision of spectral data, the observations of the influence of nuclei on the atomic spectra could be made. Figure 1.3 shows the atomic levels of caesium. By utilizing highly precise instruments, one can accurately measure these subtle changes in the spectra, allowing for the determination of various nuclear properties. It is important to
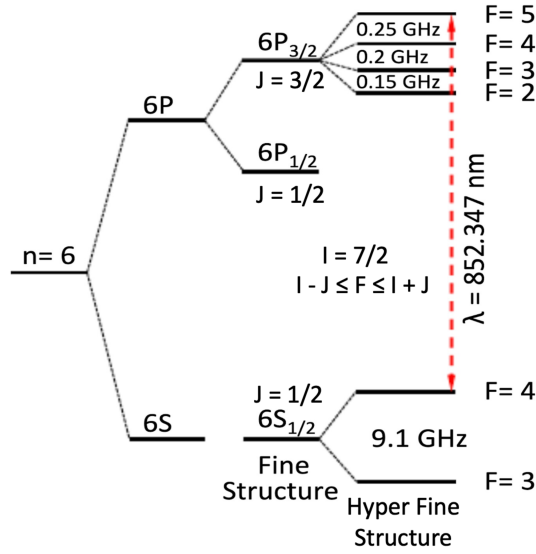
Figure 1.3: Fine and hyperfine structure of the atomic caesium. [5]

note that the measured nuclear properties obtained through such techniques are independent of any specific nuclear model. This independence arises from the consideration that the interaction between the nucleus and electrons is primarily electromagnetic and quantum mechanical in nature.

1.1.1 Isotope shift

Since the atomic nucleus is not a point object and has a finite size and mass, it shifts the fine atomic transitions. Therefore for the same isotope the transition frequencies between levels change as the nuclear mass and volume changes. Isotope shift between two isotopes of mass A and A$'$ is defined as:

$$\delta\nu_{IS}^{AA'} = \nu^{A'} - \nu^{A} \tag{1.8}$$

This shift can be divided into field shift (FS) and nuclear mass shift (MS) [19]

$$\delta\nu_{IS}^{AA'} = \delta\nu_{FS}^{AA'} + \delta\nu_{MS}^{AA'} \tag{1.9}$$

Field shift

The field shift results from changes in nuclear volume and it is primarily influenced by the distribution of nuclear charge.

The Equation 1.6 clearly illustrates the dependence of atomic spectra on the atomic number (Z). However, it is important to consider the effects arising from the fundamental properties of nuclei. These effects introduce corrections that cause unequal shifts in the energy levels.

When accounting for the finite size of the nucleus, the atomic Coulomb potential experienced by the electron takes on a different form. This can be derived using simple electrostatics by applying the equation $\vec{\nabla}.\vec{E} = \frac{\rho}{\epsilon_0}$. As a rough approximation, the nucleus can be considered as a positively charged sphere with a total charge of +Ze and a radius of R, where $R = R_o A^{1/3}$. By deriving the electric potential in two cases, for $r > R$, the potential is inversely proportional to the distance, i.e., $\frac{1}{r}$ [20]. On the other hand, for $r < R$, the potential varies proportionally to $C - (\frac{r}{R})^2$, where C represents a value that provides an indication of the potential at r=0. Figure 1.4 illustrates the variation in potential between a point-like nucleus and a nucleus with finite size.

(a) point nucleus   (b) finite size nucleus

Figure 1.4: Electric potential variation with distance(r) in point nucleus and finite size nucleus [6]

In the case of a nucleus with finite size, the boundary condition for solving the Schrodinger equation at r = 0 differs. Consequently, the wave function of the electron ($\psi(0)$) now possesses a finite value.

Using the time independent perturbation theory, an expression for shift in the energy levels from point nucleus to a finite nuclear size can be derived.
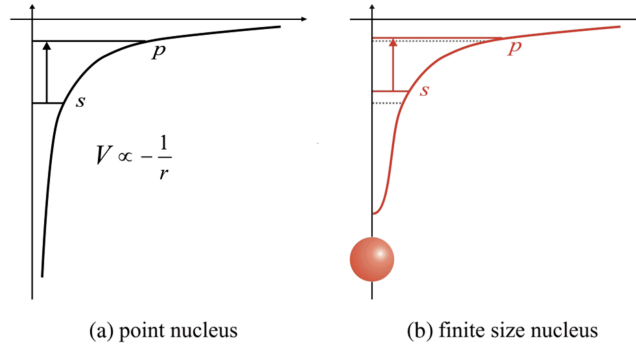
$$\delta\nu_{FNS,i\to f} = \frac{Ze^2}{6h\epsilon_o} <r_c^2> (\Delta|\psi(0)|^2)_{i\to f} \tag{1.10}$$

where

$$(\Delta|\psi(0)|^2)_{i\to f} = |\psi_f(0)|^2 - |\psi_i(0)|^2 \tag{1.11}$$

and $<r_c^2>$ is nuclear mean square charge radius which will be explained in the later part of this section.

The change in transition frequencies between two different isotopes, solely due to the field shift, can be expressed as follows:

$$\delta\nu_{FNS}^{AA'} = \frac{Ze^2}{6h\epsilon_0}\Delta|\psi(0)|^2 \times (<r_c^2>^{A'} - <r_c^2>^A) = F \times \delta <r_c^2>^{AA'} \tag{1.12}$$

The Equation 1.12 can be divided into two components: the atomic part, represented by $\Delta|\psi(0)|^2$, and the nuclear part, which depends on $\delta <r_c^2>^{AA'}$. While the field shift constant, denoted as F, is purely atomic, it does exhibit isotopic dependence. This dependence arises from the relativistic correction to the wave function at $r = 0$, which occurs as the mass of the nucleus changes. It is crucial to take this factor into account, especially for lighter isotopes. However, for heavier isotopic chains, this effect is relatively small and can be treated as a constant.

The shift in the atomic energy level is directly related to the variation in the root mean square nuclear charge radius ($\delta <r_c^2>^{AA'}$), which changes due to the addition of neutrons. The field shift primarily originates from the electrostatic interaction between the nucleus and electrons. Consequently, for electrons located far from the nuclear region (depending on the occupied orbitals), the electrostatic field remains constant across different isotopes. However, within the nuclear region, the potential differs among isotopes.

In the case of the same isotopic chain, the field shift is particularly prominent in s to p orbital transitions. Specifically, the lower energy level(s) of the heavier isotope undergo an upward shift, resulting in smaller transition energies compared to the lighter isotope [21].

Mass shift

The change in kinetic energy of the system in centre of mass (COM) frame due to the change in nuclear mass by addition of neutrons results in mass shift. This dominates the field shift for lighter nuclei ($Z < 30$). For two different isotopes A and A', the mass shift expression using momentum conservation in COM frame is given as :

$$\Delta E_{kin}^{AA'} = \frac{1}{2} \frac{M_{A'} - M_A}{M_{A'} M_A} \sum_{i=1}^{N} \overrightarrow{p}_i^2 + \sum_{i>j}^{N} \overrightarrow{p}_i \cdot \overrightarrow{p}_j \tag{1.13}$$

where $\overrightarrow{p}_i$ is the momentum of i-th electron. The first term which just depends on single electron at a time is known as normal mass shift and resembles a reduced mass correction for every isotope. The second term is a crossed term that depends on electron-electron correlations. The total mass shift can be written as,

$$\delta\nu_{MS} = \delta\nu_{SMS} + \delta\nu_{NMS} \tag{1.14}$$

Normal mass shift ($\delta\nu_{NMS}$) can be easily calculated for any atom, if its mass is known. But specific mass shift ($\delta\nu_{SMS}$) is very difficult to obtain theoretically. Mass shift does not provide any information about nuclear size parameters since it is just dependent on nuclear mass.

For a given atomic transition, the isotope shift can be expressed as,

$$\delta\nu_i^{AA'} = M_i \frac{m_A - m_{A'}}{m_{A'} m_A} + F_i \delta < r^2 >^{AA'} \tag{1.15}$$

Exploring and studying various nuclear properties provides insights into the fundamental characteristics and behaviors of nuclear systems, thereby contributing to the development and understanding of the nuclear force. This section introduces the nuclear properties relevant to laser spectroscopy.

1.1.2 Nuclear Mean Square Charge Radius

Mean square charge radius of a nucleus is defined as:

$$< r_c^2 > = \frac{\int \rho_N(r) r^2 dr^3}{\int \rho_N(r) dr^3} \tag{1.16}$$

where $\rho_N(r)$ is nuclear charge density function and $\int \rho_N(r) dr^3 = Ze$ represents the total charge. The mean square charge radius serves as a measure of the distribution of charge within the nucleus. Each moment of the nuclear charge density function provides a distinct perspective on the charge distribution.

In the first approximation nuclear density is considered constant i.e, $\rho_N(r) = \rho_N$ for r = 0 to r = R (nuclear radius) and $\rho_N(r) = 0$ for $r > R$. This leads to the expression,

$$< r_c^2 > = \frac{3}{5} R^2 \tag{1.17}$$

where $R = R_o A^{1/3}$.

The change in the mean squared radius ($\delta < r_c^2 >^{AA'}$) is influenced by three main factors. The first factor arises from the increase in the number of protons and neutrons in the nucleus, resulting in a more spread-out nuclear charge distribution and a larger value of r^2.

The second factor is associated with the deformation of the nucleus. When a nucleus becomes deformed, its charge distribution deviates from a spherical shape, leading to an increase in the value of r^2. This effect is particularly prominent in axially symmetric quadrupole deformed nuclei, where the rms value of radii can be described by the equation,

$$< r_c^2 > = < r_c^2 >_o \left(1 + \frac{5}{4\pi} \beta_2^2\right) \tag{1.18}$$

with β_2 representing the quadrupole deformation parameter and $< r_c^2 >_o$ being the mean square radius of the spherical nucleus. A well-known example of this behavior is observed in Hg isotopes, where even isotopes exhibit oblate shapes while odd isotopes display prolate shapes [22].

The third factor is related to the zero-point oscillations. A brief discussion about this can be found at [23].

For heavier nuclei, consideration must be given to higher even moments of the nuclear density function. The contribution from these higher-order terms increases with the mass of the nucleus, although it remains
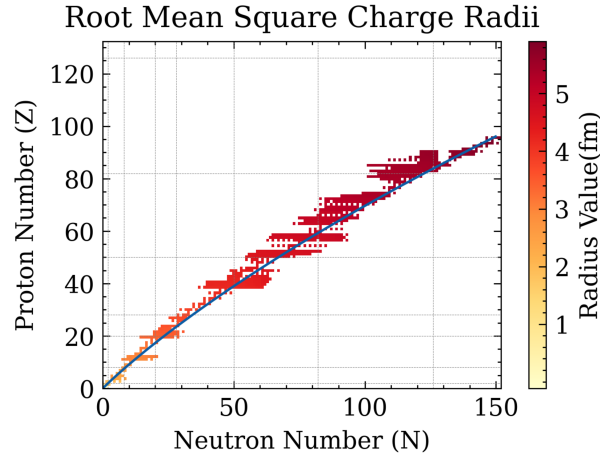
Figure 1.5: Global evolution of mean square charge radius of nuclei. Blue line corresponds to the beta stability curve. Data from [3]

relatively small, accounting for less than 8% of the overall effect. Therefore, in Equation 1.12 $\delta < r_c^2 >$ is replaced with nuclear parameter which incorporates all the higher even moments.

$$\Lambda^{AA'} = \delta < r_c^2 > + \frac{C_2}{C_1}\delta < r_c^4 > + \frac{C_3}{C_1}\delta < r_c^6 > + \ldots \qquad (1.19)$$

where C_n are tabulated Seltzer coefficients [24]. Figure 1.5 displays the experimental mean square charge radii along the nuclear chart.

1.1.3 Nuclear Spin

Nuclear spin (I) is a quantum mechanical property intrinsic to atomic nuclei, arising from the presence of protons and neutrons, which are themselves composed of quarks with inherent spin. It represents the total angular momentum of the nucleus which is composed of intrinsic angular momentum and orbital angular momentum. Therefore the nuclear spin vector can be expressed as :

$$\mathbf{I} = \sum_{i=1}^{A}(l_i + s_i) = \mathbf{L} + \mathbf{S} = \sum_{i=1}^{A} j_i \qquad (1.20)$$

where the decomposition is done according to the convenience. The nuclear spin quantum number is then given as:

$$|\mathbf{I}| = \sqrt{I(I+1)}\hbar$$
$$I_z = m_I \hbar \qquad (1.21)$$

I_z is the projection of nuclear spin along a chosen z-axis. m_I takes values from -I to +I in the steps of one unit.

Nuclei possess half-integer or integer values of spin (e.g., 1/2, 1, 3/2) depending on the mass number. This property plays an important role in determining the magnetic dipole and electric quadrupole moments measured using laser spectroscopy.

1.1.4 Nuclear Magnetic Dipole Moment

Magnetic dipole moment of the nucleus originates from the motion of charged particles that form the nucleus. The dipole term can be expressed as :

$$\mu = \frac{e\hbar}{2m}l \tag{1.22}$$

where l corresponds to the orbital angular momentum quantum number of the particle. When m is considered as mass of proton, the magnetic moment is expressed as:

$$\mu = \frac{g_l l}{\mu_N} \tag{1.23}$$

where g_l is the orbital gyromagnetic factor or g-factor of a free nucleon $g_l = 0$ for a proton and $g_l = 1$ for neutron. Accounting for intrinsic spin of nucleon in magnetic moment leads to

$$\mu = \mu_l + \mu_s = (g_l l + g_s s)\frac{\mu_N}{\hbar} \tag{1.24}$$

g_s is gyromagnetic spin factor which is different for both proton and neutron. Therefore the magnetic moment of the nucleus can be estimated as the sum of magnetic moments of individual nuclear constituents i.e,

$$\mu_I = \sum_{i=1}^{A}[g_{l,i}l_i + g_{s,i}s_i]\frac{\mu_N}{\hbar} \tag{1.25}$$

Due to the complexities in the strong nuclear force, the calculation of magnetic dipole moment is not as trivial as Equation 1.25. It does provide a good estimate when shell model is used but does not reproduce the exact experimental values [25] [26]. Figure 1.6 shows the general variation of experimental nuclear magnetic dipole moment values.
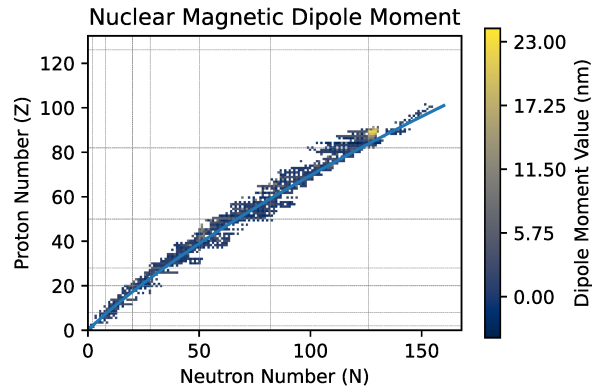
Figure 1.6: Variation of experimental magnetic dipole moment values in the units of nuclear magneton. Data from [7]

1.1.5 Nuclear Electric Quadrupole moment

Non-spherical charge distribution of nucleus leads to a non zero electric quadrupole moment. It provides an insight into the deformation of nucleus from a spherical shape. The charge distribution of a nucleus generates an electric potential depending on the nuclear charge density ($\rho(r')$). The multipole expansion of such a potential results in an expression for electric quadrupole (Q) as :

$$eQ = \int \rho(\mathbf{r}')\mathbf{r}^2(3cos^2(\theta) - 1)dv' = \int \rho(\mathbf{r}')(3z'^2 - \mathbf{r}'^2)dv' \tag{1.26}$$

where, **r** is the vector between an origin and an external point, and **r ´** is the vector defining the distance between the origin and the distribution of nuclear charges and θ is the angle between them [26]. For a spherical nucleus, quadrupole moment is zero. If $Q > 0$, then $3Z^2$ dominates as the charge density is concentrated along the z axis. Such a nucleus has a prolate shape. Negative quadrupole moment denotes that charge distribution extends along the equatorial plane perpendicular to z-axis. This results in an oblate shape. Figure 1.7 shows a pictorial representations of the shapes discussed. Nuclear shapes are also mathematically treated using spherical harmonics where Hill-Wheeler parameters are used to denote the triaxiality (γ) and deformation (β) [27]. Assuming an axial symmetry, Equation 1.18 can be used to extract β from the measurements of mean sqaure charge radii.
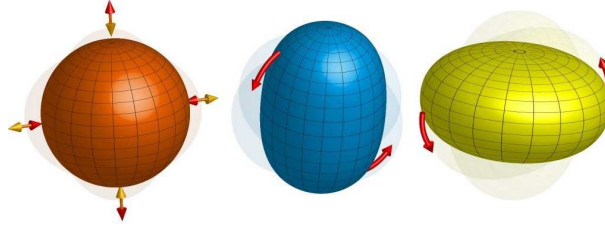
Figure 1.7: Representation of spherical (left), prolate (middle), oblate (right) nucleus. [8]

1.1.6 Hyperfine Splitting

In atomic systems, spin-orbit coupling breaks degeneracy and splits energy levels based on the total angular momentum of the electron leading to fine structure. This pure atomic phenomenon is further influenced by the interaction between nucleus and electron, resulting in the formation of hyperfine structure. The configuration of hyperfine levels is determined by the coupling of ground state spin of the nucleus (I) and the total angular momentum of the electron (J). The combined angular momentum (F) assumes values ranging from |I+J| to |I-J|, encompassing the entire range of possible values.

All of the interactions between nucleus and atomic electrons can be described using a Hamiltonian of electromagnetic multipole expansion:

$$H_{hf} = \sum_k \widehat{T^k}_N \cdot \widehat{T^k}_e \tag{1.27}$$

where $\widehat{T^k}$ are spherical tensor operations of rank k corresponding to electrons or nucleus. Even values of k are symmetry conserving electric interactions and odd ones are the magnetic interactions. Electric monopole interaction is corresponded to k=0. This causes isotope shifts discussed earlier.

Effects due to Nuclear Magnetic dipole interaction (k=1)

The magnetic field produced by the orbital motion of electrons interacts with the dipole moment of the nucleus. This leads to splitting of fine structure levels into distinct hyperfine levels.

Hamiltonian for this interaction is given as:

$$H_{hf}^{M1} = -\mu_I \cdot B_e = A \cdot I \cdot J \tag{1.28}$$

where $\mu_I = g_I \mu_N I$ with I denoting the ground state nuclear spin and μ_N is nuclear magneton and g_I is the g-factor for that spin. A denotes magnetic dipole hyperfine structure parameter and equals to $\frac{\mu B_e}{IJ}$, B_e is proportional to total angular momentum (J) of the electron. Using time independent perturbation theory, the energy difference between the split hyperfine levels can be calculated [28].

$$\frac{\Delta E_{M1}}{h} = \frac{1}{2} A \times K \tag{1.29}$$

where $K = I \cdot J = F(F+1) - I(I+1) - J(J+1)$, this accounts to coupling of nuclear and atomic angular momenta. It is clear that whenever I=0 or J=0, there is no energy level splitting due to magnetic dipole interaction.

Effects due to Nuclear Electric quadrupole interaction (k=2)

The electric quadrupole interaction term in hyperfine structure of an atom arises from the interaction between the quadrupole moment of the nucleus and the gradient of the electric field generated by the orbital electrons. The Hamiltonian for this interaction is given as:

$$H_{hf}^{E2} = B \times \frac{6(I \cdot J)^2 + 3(I \cdot J) - 2I^2 \cdot J^2}{2I(2I-1)2J(J-1)} \tag{1.30}$$

with $B = eQ_s < \frac{\partial^2 V_e}{\partial z^2} >$ being the electric quadrupole HFS parameter where Q_s is spectroscopic nuclear electric quadrupole moment (will be discussed in the later part of this subsection). The energy splitting due to this interaction is given as:

$$\frac{\Delta E_{E2}}{\hbar} = B \cdot \frac{3K(K+1) - 2I(I+1)(J+1)}{8I(2I-1)J(2J-1)} \tag{1.31}$$

It is clear that for I or $J \leq 1/2$, there is no energy level splitting due to electric quadrupole contribution.

Extraction of nuclear moments

The total energy shift in a general case of $I, J > \frac{1}{2}$ for a hyperfine level F combining both magnetic dipole and electric quadrupole interaction is given as:

$$\frac{\Delta E_{hfs}}{\hbar} = A \cdot \frac{K}{2} + B \cdot \frac{3K(K+1) - 2I(I+1)(J+1)}{8I(2I-1)J(2J-1)} \tag{1.32}$$

Therefore, in optical measurements the position of resonances relative to the centroid can be obtained using this relation:

$$\gamma = \nu + \frac{\Delta E^u - \Delta E^l}{\hbar} \tag{1.33}$$

An example of hyperfine spectra is shown in Figure 1.3. Intensity of each of the lines in the hyperfine spectra can be understood using Wigner 6J symbols. These are nothing but Clebsh Gordan coefficients when three angular momenta are added. Relative intensity or more commonly Racah intensities between the levels is given as:

$$I(F, F') = (2F+1)(2F'+1) \left\{ \begin{array}{ccc} F' & J' & I \\ F & J & 1 \end{array} \right\}^2 \tag{1.34}$$

Nuclear magnetic dipole moment and electric quadrupole moment can be thus extracted by measuring hyperfine transitions and obtaining A and B. But B_e and V_e must be obtained from atomic theory calculations. A simpler way to extract the moments is from known values using a reference isotope. Moments of stable isotopes can be measured using non optical techniques. Optical methods are necessary when exploring the isotopes far from the stability line. If the hyperfine parameters and moments of the reference isotopes (indexed as ref) are known, the moments for any isotope given their hyperfine parameters can be calculated using these relations:

$$\mu = \mu_{ref} \frac{IA}{I_{ref} A_{ref}} \tag{1.35}$$

$$Q_s = Q_{s,ref} \frac{B}{B_{ref}} \tag{1.36}$$
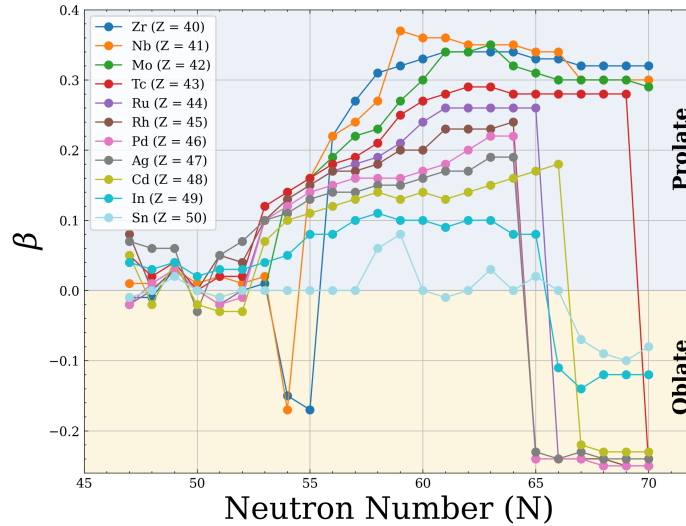
Figure 1.8: Variation of deformation parameter for nuclei from Z=40 to Z=50. Data from [9]

Hyperfine structure is only observed for odd mass nucleus because the ground state spin for all even mass nuclei is zero.

Experimentally obtained nuclear quadrupole moment (Q_s), also known as spectroscopic nuclear electric quadrupole moment can be related to the intrinsic quadrupole moment (Q) using nuclear spin (I) and its projection along the intrinsic axis of symmetry (Ω),

$$Q_s = Q\left(\frac{3\Omega^2 - I(I+1)}{(I+1)(2I+3)}\right) \tag{1.37}$$

The intrinsic quadrupole moment is related to static deformation parameter ($< \beta_2 >$), using an approximation:

$$Q \approx \frac{5ZR_o^2}{\sqrt{(5\pi)}} < \beta_2 > (1 + 0.36 < \beta_2 >) \tag{1.38}$$

where R_o^2 is mean square charge radius of a spherical nucleus. [27]

Figure 1.8 shows the trends of calculated deformation parameter in various nuclei around ^{100}Sn region. The calculations are based on the finite-range droplet macroscopic and the folded-Yukawa single-particle microscopic nuclear-structure models. It can be seen that deformation is very small around the magic number (N = 50), but it increases for neutron numbers away from magic number. It is very crucial to understand the variation and compare these values with the experimental cases to have a validation of these models.

A GUI based program was developed to simulate the spectra of any element from an optical measurement provided that ground state spins and isotope shifts are known. This program allows the user to control the FWHM, hyperfine parameters of upper and lower levels (A_l, A_u, B_l, B_u). This program was tested for the case of stable Palladium (refer to Appendix - A).

2 | Study of Pd Isotopes

As mentioned in the introduction, light Pd isotopes can be studied using the collinear set-up at Jyvaskyla [29]. The goal of this section is to acquire the skills required for analyzing this type of data in view of a future proposal. [30]. In this chapter, the data analysis for A = 102, 104, 105, 106, 108, 110 isotopes of Palladium (Z = 46) is presented [2, 29].

2.1 Experimental Details

The beam line setup used for these measurements is shown in Figure 2.1. In fluorescence laser spectroscopy, a single high-resolution laser is utilized to excite the electron from a lower atomic state to a higher state, and the resulting fluorescence signal is detected using a photon detector. In this type of spectroscopy, the laser wavelength is fixed and the velocity of the incoming beam/bunch is varied by altering the potential difference. Extraction potential of cooler buncher (V_c) is around 30 kV and a small scanning voltage (V_s) is applied over this voltage to alter the velocities of the incoming beam. This brings a Doppler shift in the laser wavelength observed by the incoming particles. When the Doppler shifted frequency matches the frequency required for the transition, the electrons are excited and the fluorescence signal is observed using a photomultiplier tube (PMT) placed near the interaction zone. Signal counts, time stamps and potential difference values are stored for further analysis.
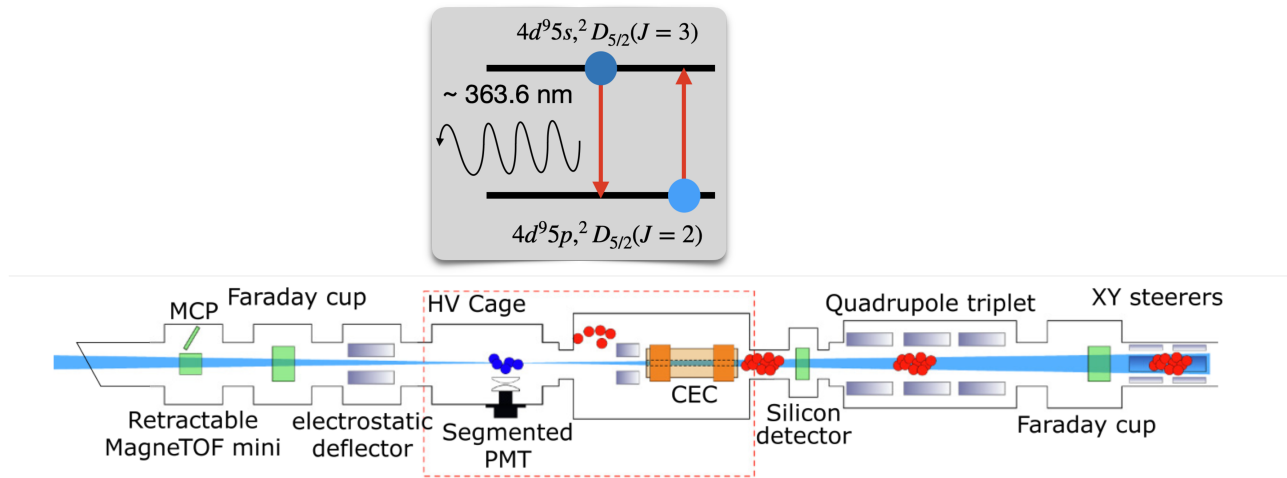
Figure 2.1: Schematic of IGISOL collinear beam line setup and the fluorescent levels involved [2]

2.1.1 Voltage Calibration and Frequency Conversion

The applied voltage for each scan is measured prior to the experiment and recorded in a calibration file. The deviation between the set voltage and the measured voltage is stored in this file. To ensure accuracy, the scanning voltages used in subsequent calculations are determined using a line of best fit between the programmed and measured voltages. Figure 2.2 illustrates an example of scanning voltage calibration. Neglecting this calibration can introduce an error into the determination of transition frequency and isotope shift, on the order of a few MHz. Previous offline measurements have shown that an additional offset of 15.1(14) V should also be taken into account after calibrating the scanning voltages [30].
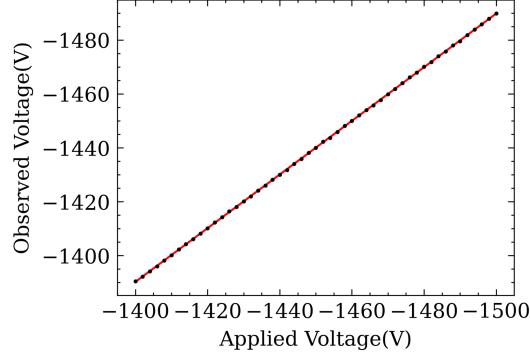
Figure 2.2: Linear calibration of set and observed scanning voltage

Laser frequency observed by incoming atoms can be calculated using relativistic mechanics and Doppler formula. The accelerated beams acquire kinetic energy from the applied voltage ($V_{acc} = V_c + V_s + 15.1$) i.e, $\frac{1}{2}mv^2 = eV_{acc}$. Doppler corrected laser frequency for the accelerated ions is given as

$$\nu = \nu_l \frac{1 \pm \beta}{\sqrt{(1 - \beta^2)}} \tag{2.1}$$

where $\beta = \frac{v}{c}$ and negative sign (-) is considered in collinear case and positive (+) in anti-collinear case. Further simplifying, we get an expression:

$$\nu = \nu_l(1 + \alpha \pm \sqrt{(2\alpha + \alpha^2)}) \tag{2.2}$$

where $\alpha = \frac{QeV_{acc}}{m_A c^2}$. In the present case Q=+1 and m_A is the mass of isotope being accelerated. The atomic transition selected for this study is $4d^9 5s,^2 D_{5/2}(J = 3)$ to $4d^9 5p,^2 D_{5/2}(J = 2)$ whose wavelength is 363.6 nm. Depending on the isotope this wavelength shifts minutely.

Figure 2.3 shows the time histogram and Doppler corrected frequency with an offset subtraction (calculated using Equation 2.2). The error in counts is calculated using Poisson distribution ($y_{err} = \sqrt{(y)}$). A time range/gate must be selected in order to find the optimal signal to noise ratio for frequency spectrum. In the case of low statistics, the gate must be chosen very carefully. Figure 2.4 shows the time gated frequency spectra by different gates. The gate represented in green gives the optimal signal to noise ratio for the frequency spectrum. A simple graphical user interface (GUI) program was made with two sliders, each corresponding to gate boundaries within which the data is considered. As the slider values are adjusted, the program dynamically displays the corresponding frequency spectra. The time range which gives a better signal to noise ratio and full width at half maximum (FWHM) can be easily tested using this program (refer to Appendix - B). Following the initial assessment with the GUI program, a more refined optimization process is conducted manually.

2.2 Data Analysis of Even Pd Isotopes: Extraction of the Charge Radii

Spectral data of aforementioned isotopes of Palladium were sorted and fit using SATLAS python package developed specially for data analysis of laser spectroscopy experiments [31]. The fit function used on the frequency data was voigt since it is a convolution of Gaussian and Lorentian profiles, each of which come from the broadening mechanisms in accelerated atoms and laser profile respectively. Chi-square minimization was used to fit the desired function to the frequency data. Statistical error in this case is a product of the
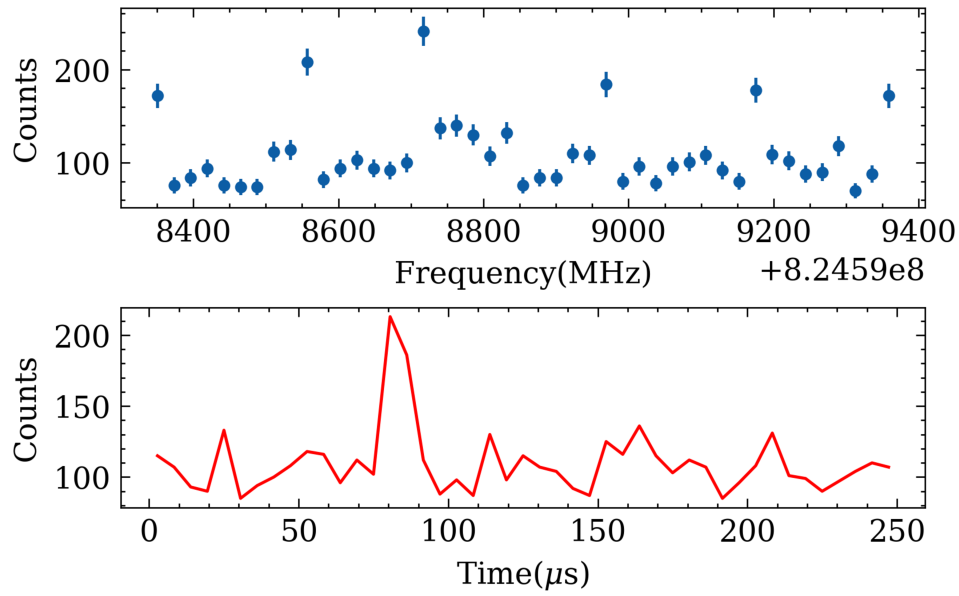
Figure 2.3: Doppler corrected frequency and time stamp histograms for one of the isotopes of Pd
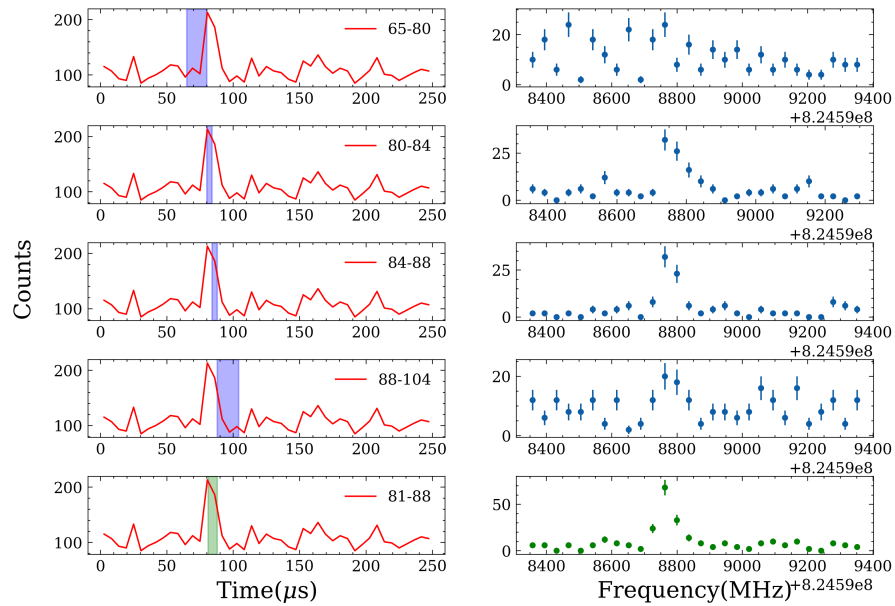

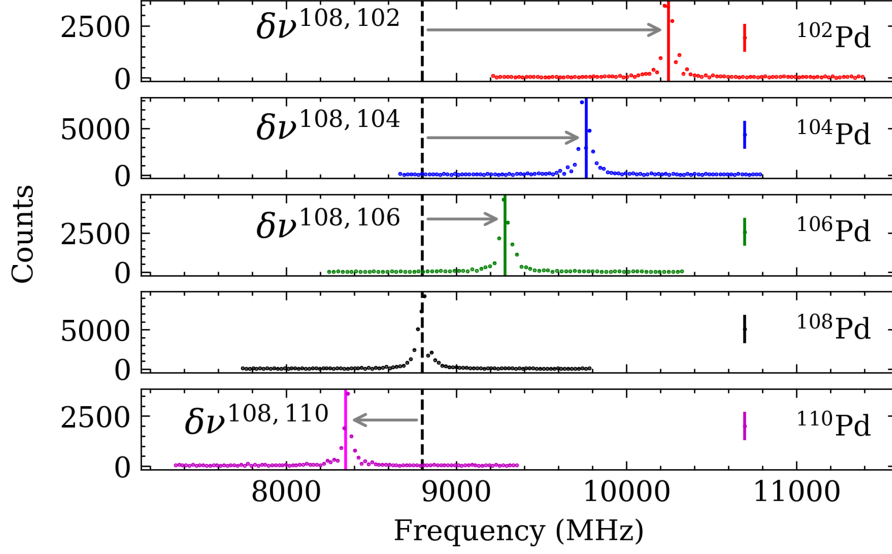Figure 2.4: Frequency data with different time gates

Figure 2.5: Frequency spectra of even Pd isotopes. Statistical errors are within the data points

parameter error that the package delivers and the reduced chi-square (chi-square × degrees of freedom) of the fit. Figure 2.5 shows the frequency data of some of the even isotopes of Pd. For each of the isotope the centroid/mean was obtained from the fit and thus isotope shift was determined.

Uncertainty Calculation

Systematic uncertainties in isotope shit are due to Radio Frequency Quadrupole (RFQ) voltage and mass of the isotope. The uncertainty in each of them is propagated to the uncertainty in isotope shift between two isotopes. The expression for this is given as

$$\triangle_{\text{sys}}(\delta\nu^{A_{\text{ref}}A}) = \nu_l \sqrt{\frac{eV_{\text{RFQ}}}{2m_{\text{ref}}c^2}} \left[\frac{1}{2}\left(\frac{\delta V_{\text{LCR}}}{V_{\text{RFQ}}} + \frac{\delta m}{m_{\text{ref}}}\right) \frac{\Delta V_{\text{RFQ}}}{V_{\text{RFQ}}} \right.$$

$$\left. + \frac{\delta V_{\text{LCR}}}{V_{\text{RFQ}}} \frac{\Delta \delta V_{\text{LCR}}}{\delta V_{\text{LCR}}} + \frac{\Delta m_{\text{ref}} + \Delta m_{\text{ref}}}{m_{\text{ref}}} \right] \quad (2.3)$$

where ν_l is the laser frequency, V_{RFQ} is voltage applied to RFQ, $\delta V_{LCR} = |V_{LCR}^{A_{ref}} - V_{LCR}^A|$ where V_{LCR} for each of the isotopes is the accelerating voltage corresponding to the centroid of the resonance peak. According to [32] $\frac{\Delta V_{RFQ}}{V_{RFQ}} = 10^{-3}$ and $\frac{\Delta \delta V_{LCR}}{\delta V_{LCR}} = 10^{-4}$, $\delta m = |m_{ref} - m_A|$ is the mass difference between reference isotope and isotope of interest and Δm is the uncertainty in mass. ^{108}Pd has been chosen as the reference isotope for the isotope shift calculations.

2.2.1 King Plot

The extraction of the mass shift factor (M) and field shift factor (F) for a specific transition can be achieved by obtaining information about the change in charge radius through non-optical methods, or vice versa. In order to eliminate the dependence on the mass of the isotope, the Equation 1.15 can be rewritten as follows:

$$\mu^{AA'}\delta\nu_i^{AA'} = M_i + F_i\mu^{AA'}\delta<r^2>^{AA'} \quad (2.4)$$

Table 2.1: Isotope shifts with statistical uncertainties in square brackets and systematic uncertainties in curved brackets

Isotope	Shift (MHz)	Literature (MHz) [29]	Charge radius (fm)	$\delta <r^2>^{108,A}$ (fm^2)
102	1443.3[6](192)	1452.8[7](190)	4.481(3)	-0.677(25)
104	951.4[14](128)	958.1[6](130)	4.506(1)	-0.453(13)
105	833.5[8](90)	839.7[9](100)	4.514(2)	-0.381(12)
106	489.2[4](64)	494.7[6](60)	4.531(3)	-0.227(8)
108	0.0	0.0	4.556(3)	0
110	-440.5[3](54)	-436.4[8](60)	4.578(2)	0.201(6)
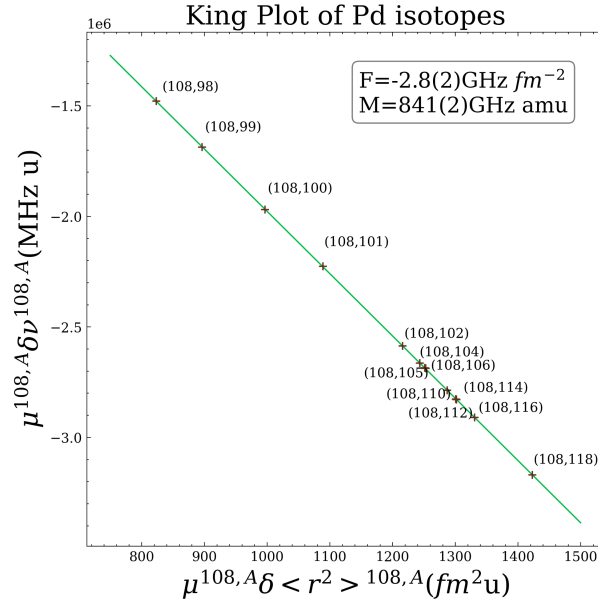
Figure 2.6: King plot for stable Pd isotopes

where $\mu^{AA'}$ or $k^{AA'}$ is the modification factor related to mass of isotopes of mass A and A'. A linear fit of $\mu^{AA'}\delta <r^2>^{AA'}$ and $\mu^{AA'}\delta\nu_i^{AA'}$ allows extraction of M and F graphically.

King plot technique was used to determine the mass and field shift factors for $4d^9 5s,^2 D_{5/2}(J = 3)$ to $4d^9 5p,^2 D_{5/2}(J = 2)$ transition. Mass and field shift factors obtained were 841(2) GHz amu and -2.8(2) GHz respectively. The correlation between the slope and intercept was also taken into consideration while obtaining the uncertainty in both the factors. A few more data points are considered in the plot using the values from [29]. These factors can be used later to calculate the mean square charge radii of other radioactive Pd isotopes.

2.3   Data Analysis of Odd ^{105}Pd Isotope: Extraction of the Hyperfine Parameters

Experimental data of ^{105}Pd was analyzed to extract the hyperfine parameters by fitting the spectra (Figure 2.7). The analysis program needs to be set with ground state spin of nuclei and the total angular momentum of electron for the transition levels. The centroid of the hyperfine spectra is the weighted average of the centroids of each of the resonance, where the weights are individual intensities. Racah intensities are calculated by the

Level	A(MHz)		B(MHz)	
	Present analysis	Literature [29]	Present analysis	Literature [29]
4d^9 5s, ^{2}D$_{5/2}$ J=3	-392.8[4]	−391.5[4]	-587.3[5]	-650[5]
4d^9 5s, ^{2}D$_{5/2}$ J=2	-85.2[5]	−82.2[5]	-259.3[4]	-302[4]

Table 2.2: Measured hyperfine parameters compared to the literature values with statistical uncertainty denoted in squared brackets
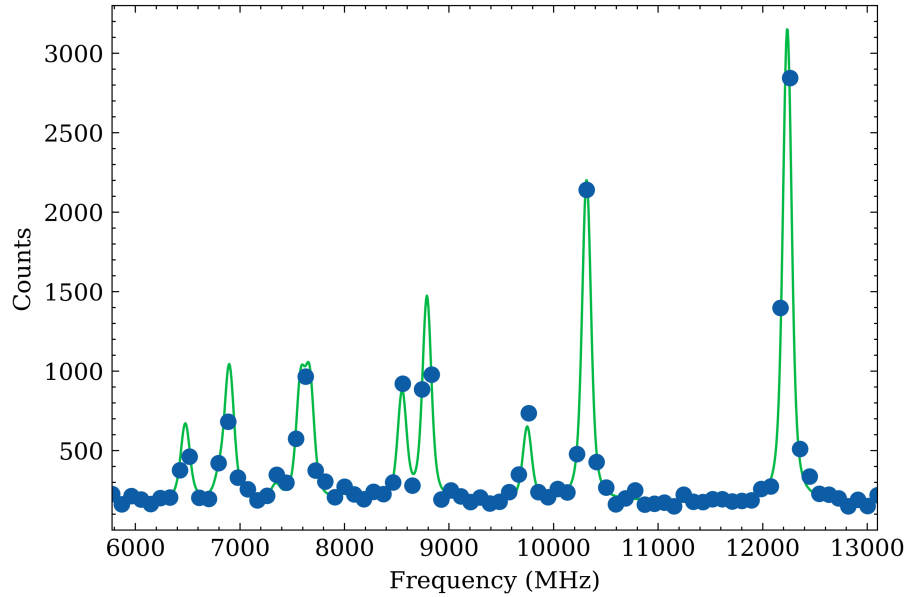

Figure 2.7: Experimental hyperfine spectra and the corresponding fit of ^{105}Pd

package depending on the given spin values for nucleus and electron.

The results are stated in Table 2.2. These hyperfine parameters and moments can be used in calculating moments for isotopes far from the stability line.

3 | Laser Alignment of a Broad Band Cavity at GISELE

The second way to study light Pd nuclei is by means of resonant ionization laser spectroscopy. It involves the absorption of photons at specific resonant frequencies to excite atoms or molecules from their ground state to higher energy states, resulting in ion production. These ions are separated from the atomic beam and detected using ion detectors. This technique requires multiple tunable lasers at different frequencies. The goal of this work is to study the sensitivities of existing laser ionization schemes of Pd for the extraction of nuclear observable by means of laser spectroscopy, particularly the development and characterization of broadband laser used for the last step of a new resonant ionization scheme.

The existing resonant ionization schemes (RIS) for Pd provide small field shift parameter for the first excited level. This results in less sensitivity in the determination of mean square charge radii. A new three level RIS (Figure 3.1) was found for Pd by Ortiz et al [2] and the sensitivity of $4d^9, (^2D_{5/2})6s$ level for hyperfine parameters and mean square radii needs to be measured.
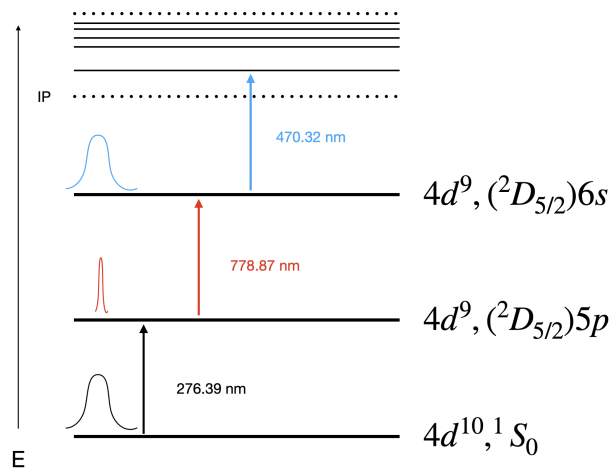
Figure 3.1: New three level resonant ionisation scheme for Pd [2]

Laser stands for Light Amplification by Stimulated Emission of Radiation. It comprises of a gain medium, a resonator, and a pump source. When light interacts with the laser gain medium, three distinct processes take place: spontaneous emission, stimulated emission, and absorption. Each of these processes is described using Einstein A and B coefficients.

3.1 Interaction of Light with Matter

Absorption is the process by which an atom in its ground state absorbs a photon of energy from the radiation field, transitioning to an excited state. The rate of change in population in the lower energy state due to absorption is described by the equation :

$$\left(\frac{dN_1}{dt}\right)_{abs} = -B_{12}N_1\rho(\nu) \tag{3.1}$$

where B_{12} is Einstein coefficient for absorption and $\rho(\nu)$ is the spectral energy density of the radiation field.

Spontaneous emission occurs when an atom in an excited energy level spontaneously emits a photon, transitioning to a lower energy state. The rate of change in population in the excited state due to spontaneous

emission is given by :

$$\left(\frac{dN_2}{dt}\right)_{spont.em} = -A_{21}N_2 \tag{3.2}$$

where A_{21} is Einstein coefficient for spontaneous emission.

Stimulated emission occurs when an atom in the presence of a radiation field is already in an excited state and is stimulated by a photon to transition to a lower energy level. This results in the emission of a second photon with the same energy and phase as the stimulating photon. The rate of change in population in the excited state due to stimulated emission is expressed as :

$$\left(\frac{dN_2}{dt}\right)_{stim.em} = -B_{21}N_2\rho(\nu) \tag{3.3}$$

where B_{21} is Einstein coefficient for stimulated emission. A schematic representation of above processes are shown in Figure 3.2.
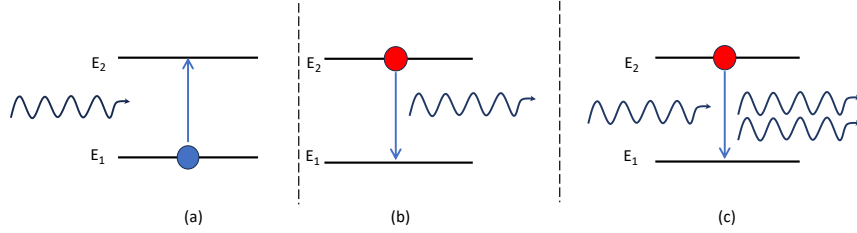

Figure 3.2: Various interactions between light and matter, (a)Absorption (b)Spontaneous emission (c) Stimulated emission

At thermal equilibrium, where there are no net changes in population, the ratio of the number of atoms in the excited state to the ground state is given by :

$$\frac{N_2}{N_1} = \frac{B_{12}\rho(\nu)}{B_{12}\rho(\nu) + A_{21}} \tag{3.4}$$

This relationship is influenced by the spectral energy density $\rho(\nu)$ and the Einstein coefficients.

Planck's law describes the spectral radiance emitted by a black-body at temperature T. The relationship between Einstein's coefficients can be derived by comparing the expression for $\rho(\nu)$ in the atomic system using Equation 3.4 and Planck's law.

$$\frac{A_{21}}{B_{21}} = \frac{8\pi\nu^2 h\nu}{c^3} \tag{3.5}$$

$$B_{21} = B_{12} \tag{3.6}$$

To achieve laser action, population inversion is required, where the number of atoms in the excited state exceeds the number in the ground state. However, in a two-level atomic system, achieving population inversion is challenging. The ratio of spontaneous emission to stimulated emission is proportional to the cube of frequency, making it more difficult to achieve population inversion at higher frequencies. To address this, additional energy levels are introduced to the system to increase the likelihood of achieving population inversion [33].

3.2   Laser Principle

In a laser system, there are two competing processes: losses caused by absorption and spontaneous emission, and amplification caused by stimulated emission. The losses can be characterized by a loss coefficient α_s,

which includes contributions from absorption, scattering, and spontaneous emission. Additionally, losses occur due to the finite reflectivity of the cavity mirrors, represented by the loss coefficient α_m. For a cavity with two mirrors separated by a round trip length $2d$, the total loss coefficient is given by

$$\alpha_m = \alpha_{m1} + \alpha_{m2} = \frac{1}{2d}\ln(R_1 R_2) \tag{3.7}$$

where R_1 and R_2 are the reflectivities of the mirrors. The total round trip loss is given by the sum of α_s and α_m, denoted as $\alpha = \alpha_m + \alpha_s$.

The amplifier gain, denoted as $\gamma_0(\nu)$, represents the amplification of the electromagnetic radiation within the laser medium. It is a measure of the increase in the intensity or power of the incident radiation as it interacts with the active medium. It is defined as the product of the equilibrium population density difference between the lasing levels ($N_0 = N_2 - N_1$) and the total cross section $\sigma(\nu)$:

$$\gamma_0(\nu) = N_0 \sigma(\nu) \tag{3.8}$$

The total cross section $\sigma(\nu)$ is a measure of interaction strength between the laser medium and the incident radiation at a specific frequency ν. It quantifies the probability per unit frequency that the transition occurs between the energy levels involved in the laser process. It is determined by the wavelength of the lasing transition λ, the spontaneous lifetime of the excited level $\tau_{sp} = \frac{1}{A_{21}}$, and the line shape function $g(\nu)$. The line shape function, denoted as $g(\nu)$, describes the spectral distribution of the electromagnetic radiation emitted or absorbed by a transition in the laser medium. It represents the probability distribution of frequencies or wavelengths associated with the transition.

To achieve lasing action, two conditions must be satisfied: the gain condition and the phase condition. The gain condition states that the gain provided by the amplifier, $\gamma_0(\nu)$, must be greater than the total loss α. The phase condition requires that the round trip phase shift, represented by $2kd$, where $k = \frac{2\pi\nu}{c}$ is the phase shift coefficient and d is the round trip length, is an integer multiple of 2π. This condition ensures constructive interference and determines the allowed resonator modes.

The pump source is responsible for creating population inversion in the laser medium, generating photons near the optical axis of the cavity. These photons undergo stimulated emission, leading to amplification of the photon field inside the cavity. The output mirror, partially transmissive, allows the transmission of light to form the laser beam. The gain condition, along with population inversion, ensures that the round trip amplification overcomes the cavity losses. The phase condition determines the transverse and longitudinal resonator modes. Incorporating wavelength-dependent losses $\alpha(\nu)$ into the resonator allows for wavelength selection in tunable lasers [33].

3.2.1 Types of Lasers

Lasers are classified based on the type of gain medium used, such as gas, liquid, solid-state, or dye. One of the earliest gain media used was ruby, which operates on a three-level system. However, three-level lasers are not very efficient and require high gain to achieve population inversion. This led to the development of (quasi) four-level lasers which are more commonly used today.

Examples of (quasi) four-level lasers include Nd:YAG (neodymium-doped yttrium aluminum garnet) and Ti:sapphire (Titanium-doped sapphire). Nd:YAG emits light primarily in the infrared region at 1064 nm and can be frequency doubled to 532 nm. The 532 nm light is often used for optical pumping of Ti:sapphire lasers. Ti:sapphire lasers have a broad emission range from 650 nm to 1100 nm, making them suitable for tunable laser applications.

Ti:sapphire gain medium consists of Ti^{3+} ions embedded in a sapphire crystal lattice. The crystal field splits the degenerate ground state of Ti^{3+} into two vibrational bands: $^2T_2$ and ^2E. Population inversion is achieved through transitions from the $^2T_2$ state to the ^2E state in the range of 420-600 nm. Figure 3.3 shows the laser scheme for Ti:sa laser. Common pump sources for Ti:sapphire lasers are frequency-doubled Nd:YLF (523 nm) or Nd:YAG (532 nm) lasers. The fast and non-radiative decays from the ^2E band to broad vibrational states in $^2T_2$ give rise to a broad fluorescence spectrum. The fluorescence lifetime at room temperature is approximately 3.2 μs [34].

Another type of laser is the dye laser, which utilizes an organic dye as the gain medium. Dye lasers have a wide tunable range and can emit light across various wavelengths. The gain medium consists of an organic dye dissolved in a liquid or solid matrix. Pumping the dye with an appropriate light source excites the dye molecules, resulting in population inversion and laser emission.

Overall, the choice of gain medium in a laser depends on factors such as the desired output wavelength, tunability, efficiency, and specific application requirements. Figure 3.4 shows the wavelength coverage of dye and Ti:sa lasers.
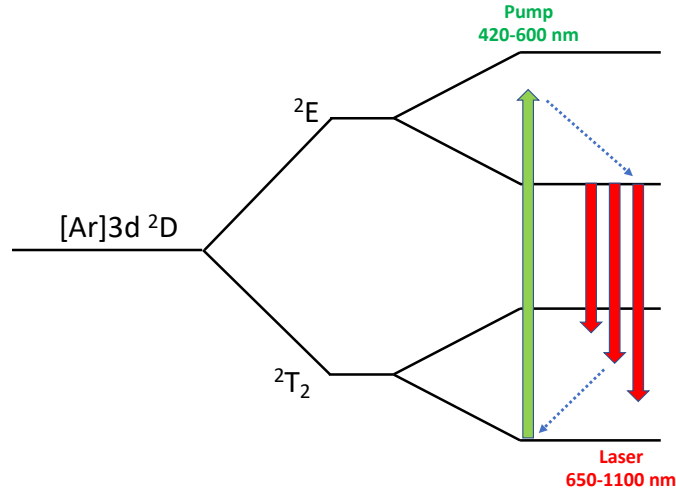

Figure 3.3: Laser scheme of Ti:sa laser, with dashed line representing fast decays
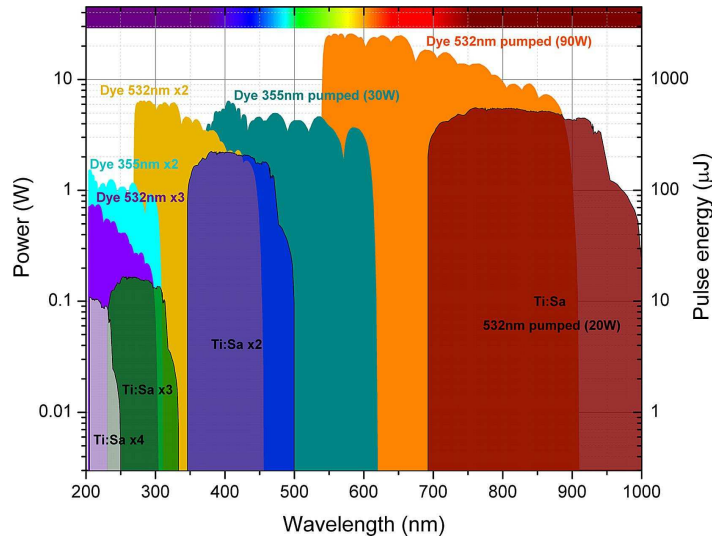

Figure 3.4: Wavelength coverage and available laser powers for Dye and Ti:sapphire-lasers
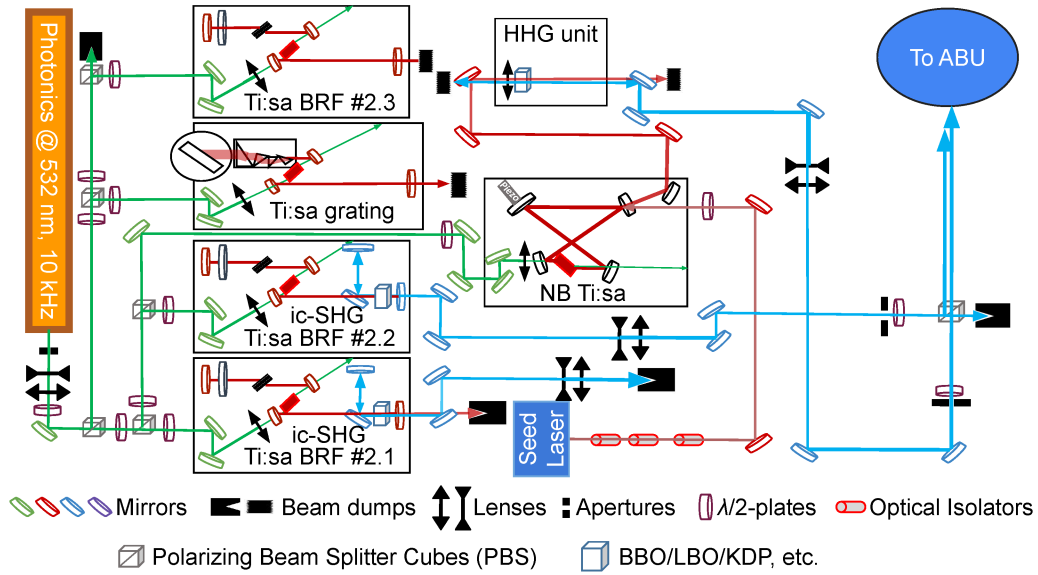
Figure 3.5: GISELE facility layout [10]

3.3   GISELE

GISELE (Ganil Ion source using Electron Laser Excitation) is an offline laser facility at Ganil, which is currently used for offline laser ionization and spectroscopy experiments. This lab facilitates the development and verification of resonant ionization schemes, hyperfine parameters and isotope shifts of stable elements. Diffused atoms are created by resistive heating in Atomic Beam Unit (ABU), which are then studied using lasers. Figure 3.5 shows the layout of the GISELE facility.

The laser system consists of Ti:sa lasers which are pumped using a frequency doubled Nd:YAG laser(532 nm) with a 10 kHz repetition rate and pulse width of ∼150 ns. The pump laser has maximum average power of 75 W which is distributed to each of the Ti:sa laser cavities using half-wave plates and polarizing beam splitter cubes.

The broadband BRF Ti:sa laser has a Z-shape resonating cavity. The bare cavity without any wavelength section elements consists of two pump mirrors, the Ti:sa crystal, focussing lens, short wave pass (SWP) curved mirrors around the crystal, one high reflection mirror (HR) and an output mirror (OC). Convex lens (CL) are used to focus the pump beam on the crystal. The Ti:sa crystal is cut at Brewster's angle. It is the angle of incidence with minimum reflection losses for p-polarised light (electric field parallel to the incident plane) [35]. The curved mirrors have transmission in shorter wavelengths (up to 532 nm) and high reflection in higher wavelength ranges (650-1050 nm). The laser cavity is optimized such that any astigmatism from surface of Ti:sa crystal and the curved mirrors cancel out each other. Figure 3.6 shows the above discussed elements.

Primary selection of wavelengths is done using frequency selective coating on cavity mirrors. Lyot filter (birefringent filter) and etalons are then used for finer wavelength output selection whose description is given below.

3.3.1   Lyot Filter:

Birefringence is a phenomenon that occurs when linearly polarized light passes through an anisotropic crystal, resulting in double refraction. The optical properties of such a crystal are influenced by its orientation relative to the incidence angle and polarization of light. When light travels along a specific direction, known as the optical axis, it passes through the medium with a single velocity, leading to conventional refraction.
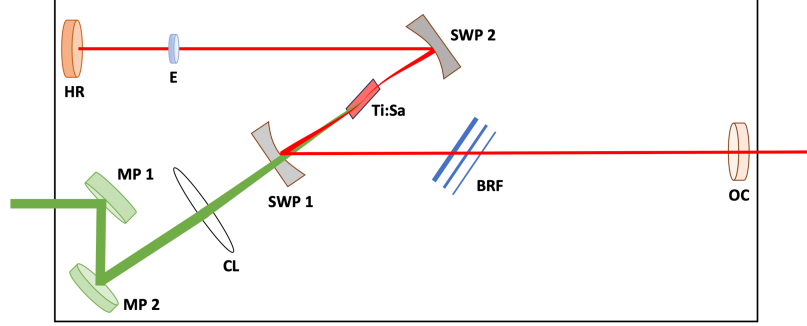
Figure 3.6: Schematic representation of broadband Ti:sa cavity

However, when light enters the crystal along a non-equivalent axis, it splits into two rays, each with mutually perpendicular polarizations.

This anisotropic crystal has the ability to transform incident Transverse Magnetic (TM) polarized light (p-polarized) into elliptical polarization, which consists of both Transverse Electric (TE)(s-polarised) and TM linear polarizations (see Figure 3.7). This transformation occurs due to the disparity in refractive index (n) between the two axes of the crystal. The refractive index along the optical axis is referred to as the ordinary index (n_o), while the index in the perpendicular direction is called the extraordinary index (n_e). This discrepancy causes a phase shift of $\delta(\lambda) = (2\pi/\lambda)(n_e - n_o)L = (2\pi/\lambda)\Delta nL$ for the transmitted light, where λ represents the wavelength and L denotes the thickness of the crystal.

Frequency selection uses this property of power loss of TM into TE polarisation. If the power transformed from TM polarisation into TE polarisation is no longer sufficient for stimulated emission, the lasing ceases for that mode. The introduction of s-polarized light into the cavity causes losses due to reflection since the intracavity elements are designed to operate with p-polarised light. For example, Ti:sa crystal is cut at Brewster angle. The transmission and free spectral range (FSR) through one plate is given as

$$T(\lambda) = T_0 cos^2(\pi\frac{\Delta nL}{\lambda}) \tag{3.9}$$

$$\Delta v_{fsr} = \frac{c}{L(n_o - n_e)} \tag{3.10}$$

Equations 3.9 and 3.10 show that a thicker birefringent crystal offers sharper filter response but the transmission maxima are closer in wavelength (reduced FSR). This problem is solved by using a stack of birefringent crystals.

A Lyot filter, also known as a birefringent filter (BRF), is composed of a series of birefringent crystals with varying thicknesses.

When N birefringent plates are considered with thickness such that the next plate has twice the thickness of the previous one, the total transmission function is given as:

$$T(\lambda) = \frac{sin^2(\frac{2^N \pi(n_e - n_o)l}{\lambda})}{2^{2N} sin^2((\frac{2^N \pi(n_e - n_o)l}{\lambda})^2)} \tag{3.11}$$

The thinnest plate (L=l) defines the free spectral range and the thickest plate (L=D) defines the spectral width:

$$\Delta\nu_{fsr} = \frac{c}{\Delta nl} \tag{3.12}$$

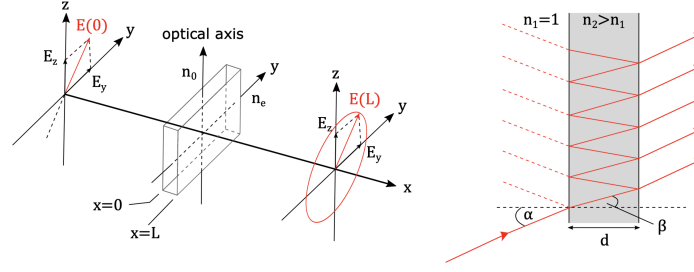$$\Delta\nu = \frac{c}{2^{N-1}}\Delta nD \tag{3.13}$$

Figure 3.7: Transformation of light in birefringent crystal (left) and the interference due to multiple reflections in etalon (right) [11]
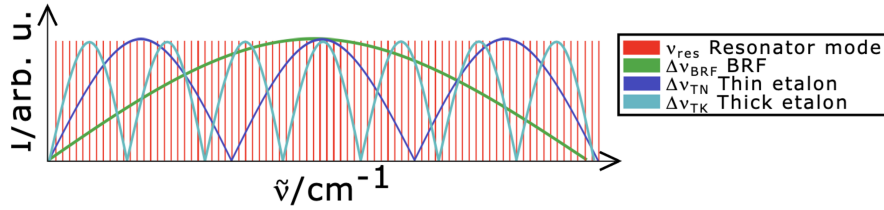

Figure 3.8: Representation of line widths of different optical elements like birefringent filter, thin and thick etalons over the Ti:sa lasing resonator modes [12]

The Lyot filter is tuned by changing the orientation of optical axis with respect to the incoming polarisation.

3.3.2   Etalon

An etalon consists of two parallel glass plates separated by distance d with partially reflecting surfaces of reflectivity R on both sides (Figure 3.7 (right)). This is also called as Fabry-Perot interferometer. A solid etalon has silica substrate between the reflecting surfaces. Each reflection inside the etalon changes the phase and the optical path length of the light. The spectral response of the etalon is governed by the interfernces between the transmitted beams. Tuning is achieved by changing the angle of the etalon with respect to the beam propagation direction (tilting), which further changes the optical path length. The transmission function of etalon is given as:

$$T_{etalon}(\nu) = T_0 \frac{1}{1 + (2\mathcal{F}/\pi)^2 sin^2[\frac{\pi\nu}{\Delta\nu_{fsr}cos\theta}]} \tag{3.14}$$

where $\mathcal{F}$ and $\Delta\nu_{fsr}$ are finesse and free spectral range(FSR) of etalon respectively.
Finesse is defined as the ratio of full width half maximum(FWHM) of the transmission peak and FSR.

$$\mathcal{F} \sim \frac{\pi\sqrt{(q)}}{2} \tag{3.15}$$

with $q = 4R/(1-R)^2$.

$$\Delta\nu_{fsr} = \frac{c}{2md} \tag{3.16}$$

where m is the resonator mode and d is the optical path length. Figure 3.8 shows a rough description of line widths of the wavelength selection elements over the laser cavity modes.
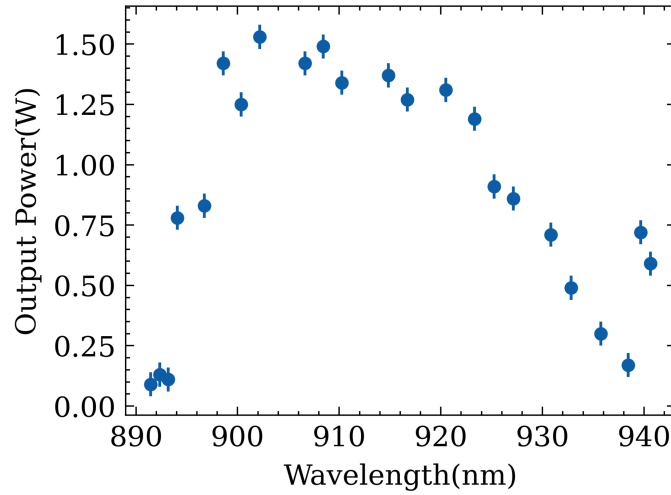
Figure 3.9: Variation of output power with the tuning wavelength

3.3.3 Cavity Alignment:

The laser cavity without any wavelength selection elements is initially aligned using a He-Ne laser (632.816 nm), which is passed from the output mirror side. Two mirrors outside the cavity allow aligning the beam spot at the center of the OC mirror and the SWP-1 curved mirror. Rest of the mirrors in the cavity are adjusted such that the He-Ne beam passes or reflects through the centre. To ensure a closed loop formation of the light beam inside the cavity, back reflections are checked and overlapped with the main light beam. This alignment is performed using a pin hole on the SWP-2 and HR arm, and by checking for back reflections outside the cavity on the SWP-1 and OC arm. The alignment is done with a He-Ne laser to ensure that the stimulated emission beam follows the same path.

The Nd:YAG laser which is set to low power (few mW) is used in adjusting the pump mirrors (MP-1 and MP-2). The adjustment is done such that it ensures the overlap of beam spots from He-Ne and the pump laser over all the mirrors and the Ti:sa crystal. This is a very crucial step to observe lasing action. After the alignment, the He-Ne laser is blocked from entering the cavity to avoid the damaged from the high power output of the pump laser. The pump beam power is increased to 12-15 W. Without disturbing the alignment that is already made, just using the pump mirrors the beam spot is scanned in vertical and horizontal directions. At the output, a photo-diode with a green filter is placed. The signal from photo-diode is displayed using an oscilloscope. When there is no lasing action, the signal observed is due to spontaneous emission. The output mirror and HR mirror can be adjusted slightly once the maximum signal is obtained. When the cavity is around the lasing threshold, a sharp peak is seen over already existing signal. At this point, the photo-diode must be quickly removed to avoid any damage due to high intensity laser output beam. After this step, the cavity alignment is optimized to get maximum output power. With the input average power of 14 W, the output power measured was 2.9 W.

Etalon is added to the cavity on the SWP-2 and HR arm. The maximum output power after insertion of etalon is 2.6 W. With the addition of BRF, the maximum output power dropped to 2 W. Coarse wavelength adjustment is done by rotating the birefringent filter. Finer selection of the wavelengths is done using the etalon. The reflection from the BRF is coupled into a fibre optic cable. This cable is connected to HighFinesse WS6-720 wave meter to measure the wavelength of the output laser beam. A study of variation of output power in the 890-940 nm wavelength range was performed (Figure 3.9) The error bars (5 mW) represent the drifts in the power meter output. The output mirror has a high transmission below 890 nm and thus lasing action can not be observed below this wavelength. The upper limit, 940 nm is due to the limited tuning range offered by the BRF and the input laser power. When the input power is increased, the gain curve covers several laser modes and higher wavelengths can be achieved. The output power is maximum in the range of
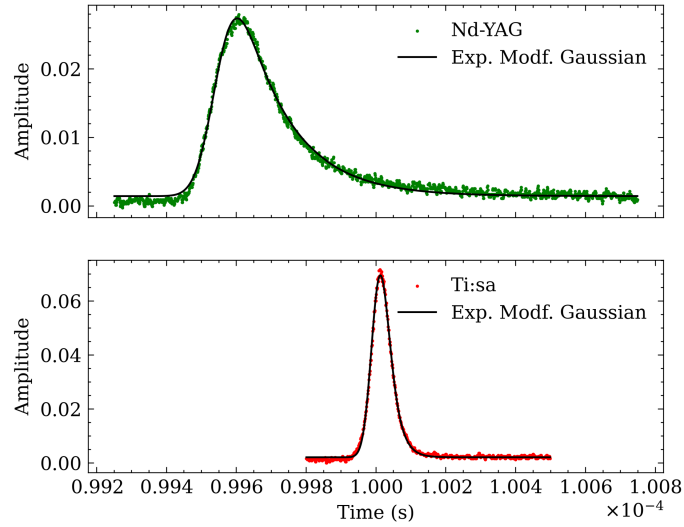
Figure 3.10: Pump and Ti:sa laser pulse characterisation

900-910 nm, which is due to high transmission of these wavelengths from BRF, etalon and OC mirror.

The pulse characterization of the input pump beam and output laser beam was conducted using a photo-diode and an oscilloscope (Tektronix-DPO 2014). The pump beam signal appeared as slightly skewed from Gaussian due to either the inherent shape of the pulse or nonlinear effects resulting from higher input intensity. Exponentially modified Gaussian function is fit to the signal, yielding pulse widths of around 110 ns. On the other hand, the output from the laser cavity exhibited a pulse width of around 50 ns (Figure 3.10). The spectral line width of the laser output, measured using the wave meter functionality, was found to be in the range of 3-5 GHz as expected. The output frequency from this laser will be doubled using an optical non-linear crystal for testing the sensitivity of the new RIS scheme.

4 | Multi-Reflection Time of Flight spectrometer: PILGRIM

This chapter is focused on the software development for online data acquisition and analysis of Time of Flight (ToF) data from PILGRIM. Super Separator Spectrometer Low-Energy Branch (S3-LEB) is a multi-stage system that incorporates Rare Elements in-Gas Laser Ion Source and Spectroscopy (REGLIS3) and a high-resolution mass spectrometer (PILGRIM). REGLIS3 consists of a gas cell where thermalization and neutralization of the heavy-ion beam occur, and reaction products are transported through a de Laval nozzle. To selectively and efficiently ionize the desired atoms, a high-power laser system with a narrow bandwidth is employed. The gas cell allows direct extraction of singly-charged ions and enables high spectral resolution measurements using resonant ionization of isotopes in the gas jet. A radio frequency ion guide captures and efficiently transports the photo-ions to a low-pressure zone, ensuring good emittance before injection into a quadrupole mass filter. Subsequent to this mass filtering, the ions are bunched and accelerated. This is followed by a Multi- Reflection Time-of-Flight Mass Spectrometer (MR-ToF MS) for high resolution mass measurements called Piège à Ions Linéaire du GANIL pour la Résolution des Isobares et la mesure de Masse (PILGRIM). Laser spectroscopy involves scanning the laser frequency while observing the number of photo-ions, emitted radiation or the mass spectra of the ions.

REGLIS3 offers high efficiency, selectivity, minimal time delay, and spectral resolution down to 200 MHz, enabling the study of nuclei in small quantities, suppression of unwanted isotopes, investigation of short-lived isotopes, and determination of isotope/isomer shifts and hyperfine structures. The expected total efficiency ranges from 4% to 24%. S3-LEB facilitates ground state property measurements, including charge radii, electromagnetic moments, and nuclear spins, providing insights into nuclear structure, collective properties, deformation, shape coexistence, and shell effects.

Additionally, S3-LEB can provide pure radioactive ion beams for low-energy mass measurements and beta decay studies. This facility is currently under offline commissioning at LPC Caen [12, 36, 37].

4.1 PILGRIM MR-ToF MS

Mass spectrometry is an analytical technique to determine the mass-to-charge ratio of ions or molecules. It involves the acceleration of charged particles using electric or magnetic fields, and in some cases, a combination of both, as its fundamental principle. In the context of this study, the relativistic expression of Lorentz's law is of particular importance. It is given by the equation:

$$\frac{d(\gamma \vec{v})}{dt} = \frac{q}{m_o}(\vec{E} + \vec{v} \times \vec{B}) \tag{4.1}$$

This equation describes the motion of charged particles in electromagnetic fields, where γ represents the relativistic factor, $\vec{v}$ denotes the velocity, q is the charge of the particle, m_o represents its rest mass, and $\vec{E}$ and $\vec{B}$ represent the electric and magnetic fields, respectively. The resolving power of a mass spectrometer is measure of its ability to distinguish two species with very close $\frac{q}{m_o}$ values.

The time-of-flight spectrometer is a widely used device for accurately determining the mass-to-charge ratio of ions. Its operational principle is based on measuring the time it takes for ions to travel a certain distance after being accelerated by a potential.

In the ToF spectrometer, ions with charge (q) are initially accelerated by a potential U, resulting in a kinetic energy $K = qU$. The time-of-flight of an ion in a field-free region over a distance(D) can be calculated using the equation:

$$ToF = \frac{D}{v} = D\sqrt{\frac{m}{2qU}} \tag{4.2}$$

The ToF of ions depends on their mass-to-charge ratio. Heavier ions with the same charge exhibit longer ToF, while ions with higher charges have a shorter ToF. By precisely measuring the time difference between
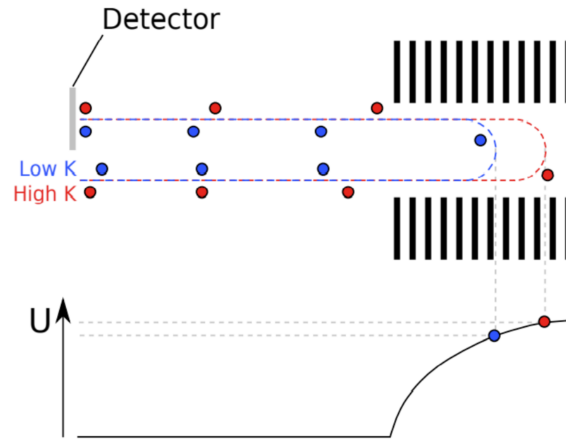
Figure 4.1: Operating principle of the reflectron [13]

the START and STOP signals, which represent the ion acceleration and detection times, respectively, the mass-to-charge ratio of ions can be determined. For a ToF spectrometer, the resolving power is given as :

$$R = \frac{m}{\Delta M} = \frac{T}{2\Delta T} \tag{4.3}$$

During the process of bunch acceleration, there is a possibility of kinetic energy dispersion, especially at lower energies. This dispersion has an impact on the spectrometer's resolving power. To address this issue, a reflectron is employed. The reflectron, which consists of multiple blades with varying potentials, is an electrostatic mirror. Ions with higher kinetic energies exhibit greater penetration into the reflectron, resulting in a slightly longer path to reach the detector. Conversely, ions with lower kinetic energies, but the same mass-over-charge ratio, experience shallower penetration into the reflectron and travel a shorter path to the detector. This is thematically shown in Figure 4.1 This principle forms the core of MR-ToF MS, where PILGRIM utilizes two sets of five electrostatic mirrors. By increasing the time-of-flight of ions through multiple reflections using these electrostatic mirrors, the necessary resolving power is achieved. PILGRIM has a resolving power up to 10^5 and a mass measurement accuracy up to the order of around 10^{-7}. A detailed explanation of PILGRIM can be found here [13].

4.2 Online ToF Data Acquisition Software

An Online ToF data acquisition software for PILGRIM was built using python. It uses the latest Atomic Mass Evaluation - AME2020 database for ToF calculations [38]. Initially an ion of reference is defined and using the ToF data of this ion, the MR-ToF MS is calibrated. Prior to the experimental procedure, simulations are performed to obtain ToF values for shoot through and different trapping times.

The steps involved in the experimental calibration process are :

1. Initially, the ions are shot through the PILGRIM without trapping (shoot through mode). These ions are detected using MagneToF (a sub-nanosecond ToF detector) [39], which yields mean ToF information (t_M).

2. The next steps involve trapping ions for one or more number of turns. This allows the calculation of estimated revolution time(ERT).

The total ToF is the sum of trapping time and mean ToF for a given ion.

$$t_T = T_{tr} + t_M \tag{4.4}$$

The estimated revolution time for a given ion for any two number of turns is defined as:

$$ERT = \frac{t_{T_i} - t_{T_{i-1}}}{N_i - N_{i-1}} \tag{4.5}$$

The fractional part of ratio between trapping time and ERT is defined as the phase of the ion($\phi_{N=0}$) for any given number of turns i.e, X_N mod 1 where,

$$X_N = \frac{T_{tr}}{ERT} \tag{4.6}$$

If the ERT of the reference ion is known, for any other isotopes of interest the ERT can be calculated as:

$$ERT_{int} = ERT_{ref} \times \sqrt{\frac{M_{int}}{M_{ref}}} \tag{4.7}$$

The phase advance of ions of interest outside the trapping cycle(ϕ_N) is given as the fractional part of $X_{N=0}$ i.e, $X_{N=0}$ mod 1 where,

$$X_{N=0} = t_M \times \frac{1 - \frac{M_{int}}{M_{ref}}}{ERT_{int}} \tag{4.8}$$

The difference in mean ToF between the reference isotope and the isotope of interest is given as:

$$dT = -(\phi_N + \phi_{N=0}) \times ERT_{int} \tag{4.9}$$

The mean ToF for any ion of interest can now be given as:

$$t_{M_{int}} = t_{M_{ref}} + dT \tag{4.10}$$

The online acquisition software enables mean ToF calculations for diverse radioactive species, with the resulting ToF values represented as vertical lines overlaid on experimental data. Users have the flexibility to select radioactive elements from the nuclear chart and include radioactive molecular species (referred to as impurities) for ToF calculations. The software supports stoichiometry, allowing users to specify the mass number of each element within a molecule. The refresh rate of online data acquisition during experiments is determined by the beam current feature. Isomeric species can also be entered with their respective excitation energies. The yield file, which contains beam production yield details from the S3 facility, facilitates the determination of peak heights for calculated ToF values. The software has been tested using ToF data for different turns in the spectrometer, and Figure 5.3 (Appendix - C) illustrates the software window during a test with 1000 turns. The calculated ToF values closely match the experimental ToF peaks, with any minor discrepancies attributed to temperature fluctuations.

The software includes a double slider feature that allows users to select an experimental ToF peak and perform a Gaussian function fit (Figure 5.4 Appendix - C). In addition, the software will be enhanced with additional features, such as phase visualization and EPICS control, in future updates [40].

5 | Conclusions and Perspectives

In conclusion, this report briefly discusses the laser spectroscopy techniques in nuclear physics. These are capable of precisely investigating minute changes in atomic transitions and thus enabling the study of various nuclear properties through measurements of isotope shift and hyperfine parameters.

The emphasis on ^{100}Sn and the N = Z line has highlighted the importance and complexities involved in studying these regions. This focus has drawn attention to the role of shell effects in shaping nuclear properties, including the observed variations in nuclear charge radii. Furthermore, given the position of Pd between Sn and Zr, it becomes intriguing to investigate whether collective or single-particle effects dominate in this intermediate region.

The development of hyperfine spectra simulator helps in the planning of experiments. It aids in understanding the achievable experimental resolution and determining the necessary measurement resolution for anticipated hyperfine parameters of a given element. Additionally, the report includes the data analysis of Pd isotopes from fluorescence laser spectroscopy technique. The variation in mean square charge radii of these isotopes was determined using King plot. Hyperfine parameters were determined from ^{105}Pd spectrum.

Characterization and development of a broadband laser cavity for investigating new resonant ionization scheme for Palladium and working principles of several optical elements was also illustrated.

Furthermore, the development of a user-friendly GUI for the PILGRIM MR-ToF MS system improves the data acquisition and analysis capabilities in online experiments.

The future perspectives of this report involve testing of new Pd ionization scheme for sensitivity in isotope shift and hyperfine parameters utilizing the tools developed in this report. This can lead to a creation of a comprehensive research proposal for conducting experiments related to neutron deficit Pd isotopes using the newly developed resonant ionization scheme. These experiments will involve the utilization of the collinear laser spectroscopy technique within a hot cavity catcher setup.

Additionally, a rigorous testing and refinement of the graphical user interface (GUI) for the MR-ToF MS will be undertaken. The testing phase will involve a comprehensive examination of functionality and performance of the GUI under various experimental conditions. It will be optimised for efficiency, responsiveness, and robustness. Any identified issues or glitches will be thoroughly addressed and resolved to ensure smooth operation during experimental sessions.

Appendix - A

Hyperfine Spectra Simulator

A GUI based program (Figure 5.1) was developed to simulate the spectra of any element from an optical measurement provided that ground state spins and isotope shifts are known. This program allows the user to control the FWHM, hyperfine parameters of upper and lower levels (A_l, A_u, B_l, B_u). This program was tested for the case of stable Palladium (^{105}Pd is the only odd isotope for stable Pd).

There is a two-fold utility to this simulator. Firstly, when the achievable experimental resolution of a specific technique is understood, it provides insight into the range of measurable hyperfine parameters. Secondly, for a given element, if the anticipated hyperfine parameters are known, the simulator helps determine the necessary measurement resolution
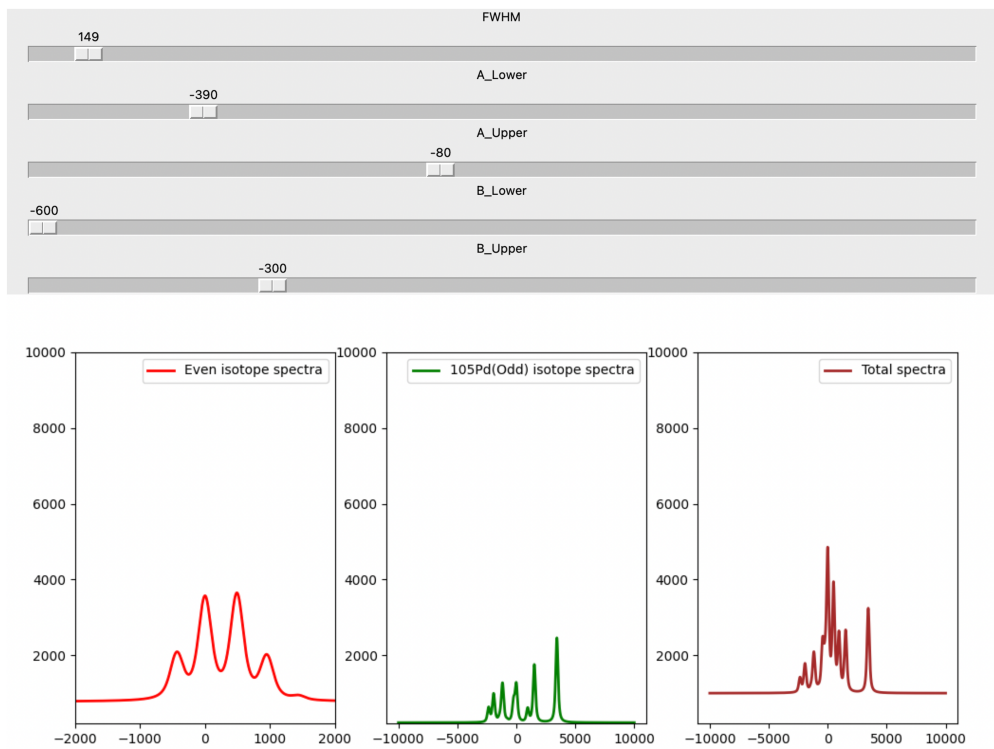

Figure 5.1: GUI based simulation of hyperfine and total spectra of stable isotopes of Pd

Appendix - B

Slider GUI for gate selection

This GUI program allows the user to select the range in the time histogram and the corresponding frequency spectra is displayed. As the slider values are updated, the frequency spectra is refreshed to correspond to the new time range. A screenshot of this GUI is shown in Figure 5.2.
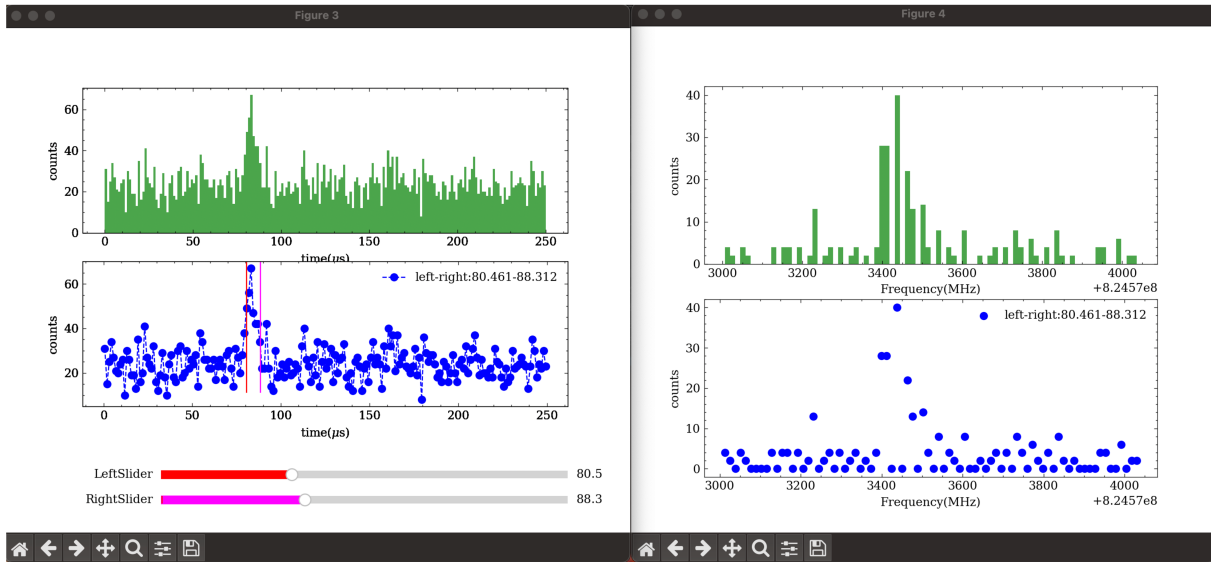

Figure 5.2: The left window shows the time data as histogram(top) and a scatter plot of bin centres(bottom). The frequency data is plotted similarly on right. Frequency spectrum gets updated when the sliders are adjusted
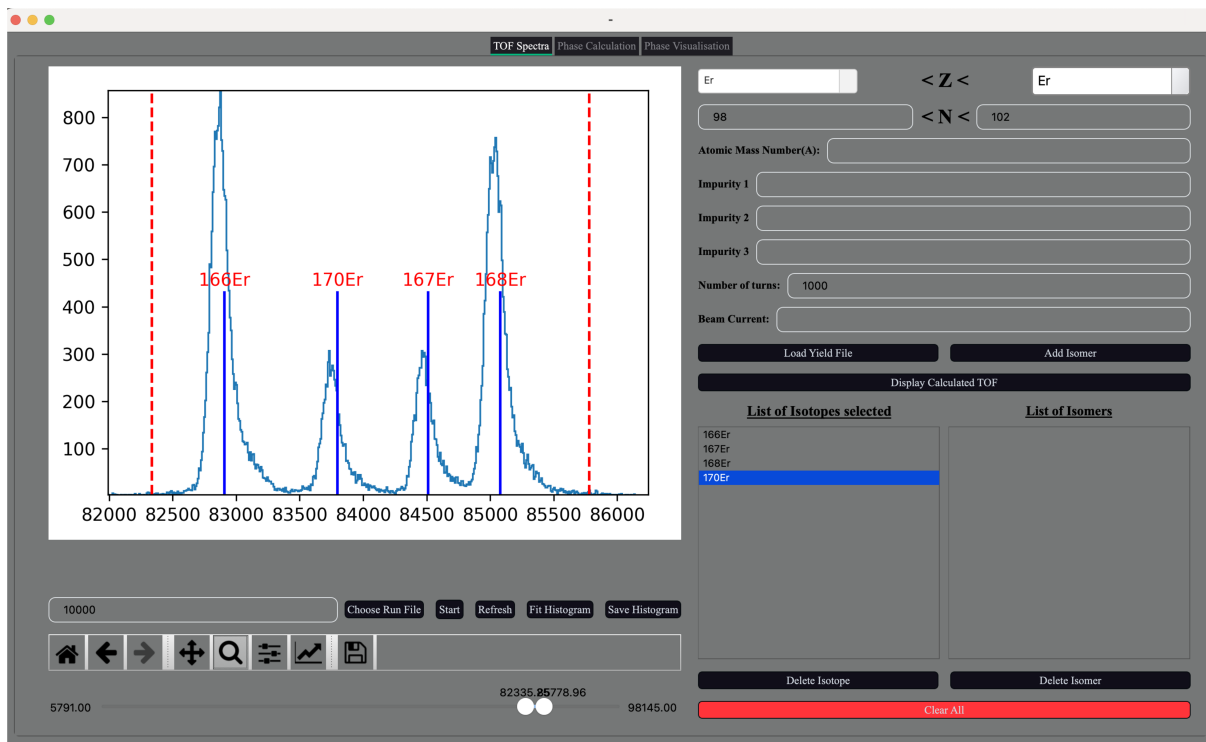
Appendix - C

Figure 5.3: Screenshot of the window displaying the online acquisition software for PILGRIM
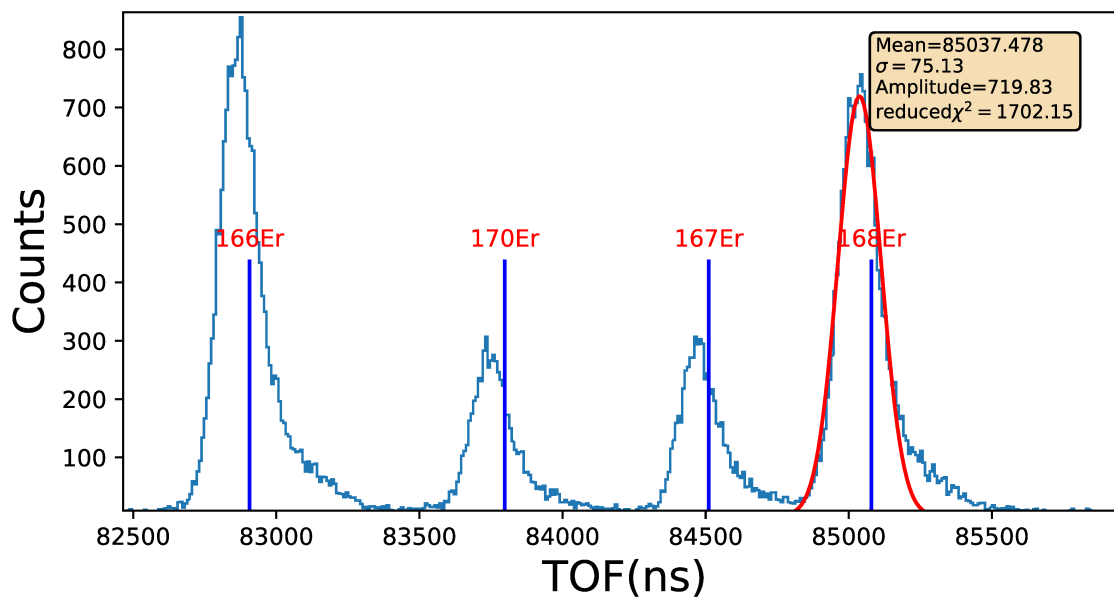

Figure 5.4: Gaussian fit of a single experimental ToF peak

Bibliography

[1] XF Yang, SJ Wang, SG Wilkins, and RF Garcia Ruiz. Laser spectroscopy for the study of exotic nuclei. *Progress in Particle and Nuclear Physics*, page 104005, 2022.

[2] Alejandro Ortiz Cortes. Palladium: a study of nuclear deformation of a refractory element. laser spectroscopy at the igisol (jyväskylä, finland) and s3-leb (ganil, france). *JYU dissertations*, 2023.

[3] István Angeli and Krassimira Petrova Marinova. Table of experimental nuclear ground state charge radii: An update. *Atomic Data and Nuclear Data Tables*, 99(1):69–95, 2013.

[4] M Reponen, RP de Groote, L Al Ayoubi, O Beliuskina, ML Bissell, P Campbell, L Cañete, B Cheal, K Chrysalidis, C Delafosse, et al. Evidence of a sudden increase in the nuclear size of proton-rich silver-96. *Nature Communications*, 12(1):4596, 2021.

[5] Syed Abdullah Aljunid, Eng Aik Chan, Giorgio Adamo, Martial Ducloy, David Wilkowski, and Nikolay I Zheludev. Atomic response in the near-field of nanostructured plasmonic metamaterial. *Nano letters*, 16(5):3137–3141, 2016.

[6] Z-T Lu, P Mueller, GWF Drake, W Nortershauser, Steven C Pieper, and Z-C Yan. Colloquium: Laser probing of neutron-rich nuclei in light atoms. *Reviews of Modern Physics*, 85(4):1383, 2013.

[7] NJ Stone. Table of nuclear magnetic dipole and electric quadrupole moments. *Atomic Data and Nuclear Data Tables*, 90(1):75–176, 2005.

[8] Silicon double magic riken. `https://www.riken.jp/en/news_pubs/research_news/rr/7240/index.html`. (Accessed on 07/06/2023).

[9] P Möller, Arnold John Sierk, Takatoshi Ichikawa, and Hiroyuki Sagawa. Nuclear ground-state masses and deformations: Frdm (2012). *Atomic Data and Nuclear Data Tables*, 109:1–204, 2016.

[10] Jekabs Romans, Anjali Ajayakumar, Martial Authier, Frederic Boumard, Lucia Caceres, Jean-François Cam, Arno Claessens, Samuel Damoy, Pierre Delahaye, Philippe Desrues, et al. First offline results from the s3 low-energy branch. *Atoms*, 10(1):21, 2022.

[11] Dominik Studer. *Probing atomic and nuclear structure properties of promethium by laser spectroscopy*. PhD thesis, Johannes Gutenberg-Universität Mainz, 2020.

[12] Jekabs Romans, Pieter Van Duppen, and Rafael Ferrer Garcia. Development and characterization of the s3-low energy branch for laser spectroscopy studies of exotic nuclei. 2023.

[13] Pierre Chauveau. *Design, simulations and test of a Time-of-Flight spectrometer for mass measurement of exotic beams from SPIRAL1/SPIRAL2 and γ-ray spectroscopy of N= Z nuclei close to ^{100}Sn*. PhD thesis, Université de Caen Normandie, 2016.

[14] Ronald Fernando Garcia Ruiz. Laser spectroscopy of exotic neutron-deficient indium (z= 49) isotopes: approaching n= 50. Technical report, 2017.

[15] Mickaël Dubois, O Bajeat, C Barué, V Bosquet, P Chauveau, S Damoy, R Frigot, S Hormigos, P Jardin, N Lechartier, et al. Radioactive and stable ion beam production at ganil. In *Journal of Physics: Conference Series*, volume 2244, page 012070. IOP Publishing, 2022.

[16] Zhihao Gao, Andreas Solders, Ali Al-Adili, Simone Cannarozzo, Mattias Lantz, Heikki Penttilä, and Stephan Pomp. New design and simulation of the ion guide for neutron-induced fission products at the igisol facility. In *EPJ Web of Conferences*, volume 284. EDP Sciences, 2023.

[17] Arne Johnson. Nuclear structure in the vicinity of the n= z line in the a= 90-100 region. *The European Physical Journal A-Hadrons and Nuclei*, 13:9–14, 2002.

[18] Brian Harold Bransden and Charles Jean Joachain. *Physics of atoms and molecules*. Pearson Education India, 2003.

[19] Robert Muller Andrey Surzhykov. Isotope shifts - nuclear mass and size effects on atomic structure. `https://www.ptb.de/cms/fileadmin/internet/institute/fpm/QMatter_2019/VL06.pdf`, 2018. (Accessed on 03/21/2023).

[20] A Adamu, YH Ngadda, M Hassan, and DI Malgwi. The coulomb energy of finite size nucleus from the study of classical electrodynamics theory. *NIPES Journal of Science and Technology Research*, 2(3):272–282, 2020.

[21] VV Flambaum, AJ Geddes, and AV Viatkina. Isotope shift, nonlinearity of king plots, and the search for new particles. *Physical Review A*, 97(3):032510, 2018.

[22] S Sels, T Day Goodacre, BA Marsh, Alessandro Pastore, W Ryssens, Y Tsunoda, N Althubiti, B Andel, AN Andreyev, Dinko Atanasov, et al. Shape staggering of midshell mercury isotopes from in-source laser spectroscopy compared with density-functional-theory and monte carlo shell-model calculations. *Physical Review C*, 99(4):044306, 2019.

[23] J Billowes and P Campbell. High-resolution laser spectroscopy for the study of nuclear sizes and shapes. *Journal of Physics G: Nuclear and Particle Physics*, 21(6):707, 1995.

[24] E. C. SELTZER. k x-ray isotope shifts. *Phys. Rev.*, 188:1916–1919, Dec 1969.

[25] Kenneth S Krane. *Introductory nuclear physics*. John Wiley & Sons, 1991.

[26] Ross Mathieson. *Charge Radii Measurements of Chromium Nuclei by Laser Spectroscopy at IGISOL-IV*. PhD thesis, University of Liverpool, 2023.

[27] R Neugart and G Neyens. Nuclear moments. *The Euroschool Lectures on Physics with Exotic Beams, Vol. II*, pages 135–189, 2006.

[28] XF Yang, SJ Wang, SG Wilkins, and RF Garcia Ruiz. Laser spectroscopy for the study of exotic nuclei. *Progress in Particle and Nuclear Physics*, page 104005, 2022.

[29] Sarina Geldhof. Developments for high-resolution laser spectroscopy and application to palladium isotopes. *JYU dissertations*, 2020.

[30] R.P. de Groote, A. de Roubin, P. Campbell, B. Cheal, C.S. Devlin, T. Eronen, S. Geldhof, I.D. Moore, M. Reponen, S. Rinta-Antila, and M. Schuh. Upgrades to the collinear laser spectroscopy experiment at the igisol. *Nuclear Instruments and Methods in Physics Research Section B: Beam Interactions with Materials and Atoms*, 463:437–440, 2020.

[31] Wouter Gins, Ruben P de Groote, Mark L Bissell, C Granados Buitrago, Rafael Ferrer, Kevin M Lynch, Gerda Neyens, and Simon Sels. Analysis of counting data: Development of the satlas python package. *Computer Physics Communications*, 222:286–294, 2018.

[32] P. Campbell, H. L. Thayer, J. Billowes, P. Dendooven, K. T. Flanagan, D. H. Forest, J. A. R. Griffith, J. Huikari, A. Jokinen, R. Moore, A. Nieminen, G. Tungate, S. Zemlyanoi, and J. Äystö. Laser spectroscopy of cooled zirconium fission fragments. *Phys. Rev. Lett.*, 89:082501, Aug 2002.

[33] Wolfgang Demtröder. *Laser spectroscopy*, volume 2. Springer, 1982.

[34] Katerina Chrysalidis. *Improving the Spectral Coverage and Resolution of the ISOLDE RILIS*. PhD thesis, Mainz U., 2019.

[35] DR Preuss and JL Gole. Three-stage birefringent filter tuning smoothly over the visible region: theoretical treatment and experimental design. *Applied optics*, 19(5):702–710, 1980.

[36] Yu Kudryavtsev, Philip Creemers, Rafael Ferrer, C Granados, LP Gaffney, Mark Huyse, Evgeny Mogilevskiy, Sebastian Raeder, Simon Sels, Piet Van Den Bergh, et al. A new in-gas-laser ionization and spectroscopy laboratory for off-line studies at ku leuven. *Nuclear Instruments and Methods in Physics Research Section B: Beam Interactions with Materials and Atoms*, 376:345–352, 2016.

[37] Jekabs Romans, Anjali Ajayakumar, Martial Authier, Frederic Boumard, Lucia Caceres, Jean-François Cam, Arno Claessens, Samuel Damoy, Pierre Delahaye, Philippe Desrues, et al. High-resolution laser system for the s3-low energy branch. *Nuclear Instruments and Methods in Physics Research Section B: Beam Interactions with Materials and Atoms*, 536:72–81, 2023.

[38] Meng Wang, WJ Huang, Filip G Kondev, Georges Audi, and Sarah Naimi. The ame 2020 atomic mass evaluation (ii). tables, graphs and references. *Chinese Physics C*, 45(3):030003, 2021.

[39] 1. `http://www.cromlab.es/Articulos/SGE/ETP/TA/TA-0129-A.pdf`. (Accessed on 07/07/2023).

[40] Epics - experimental physics and industrial control system. `https://epics-controls.org/`. (Accessed on 07/07/2023).